Spring 5-2016

Development and Validation of an Empirical Temperature-Dependent Voltage Model for Diode Laser Characterization

Grant Matthew Brodnik
Rose-Hulman Institute of Technology

Development and Validation of an Empirical Temperature-Dependent Voltage Model for Diode Laser Characterization

A Thesis

Submitted to the Faculty

of

Rose-Hulman Institute of Technology

by

Grant Matthew Brodnik

In Partial Fulfillment of the Requirements for the Degree

of

Master of Science in Optical Engineering

May 2016

ROSE-HULMAN INSTITUTE OF TECHNOLOGY

Final Examination Report

Grant M. Brodnik	Optical Engineering
Name	Graduate Major

Thesis Title: Development and Validation of an Empirical Temperature Dependent Voltage Model for Diode Laser Characterization

DATE OF EXAM: August 22, 2016

EXAMINATION COMMITTEE:

	Thesis Advisory Committee	Department
Thesis Advisor:	Paul Leisher	PHOE
	Jeffery Leader	MA
	Richard Liptak	PHOE
	Wonjong Joo	SNUST

PASSED X **FAILED**

ABSTRACT

Brodnik, Grant Matthew
M.S.O.E Dual Degree
Rose-Hulman Institute of Technology
May 2016

Development and Validation of an Empirical Temperature-Dependent Voltage Model for Diode Laser Characterization

Thesis Advisor: Dr. Paul O. Leisher

Keywords: Broad area laser diodes, eye-safe, resonant pumping, high-power, high-efficiency, InP-based, parametric models, cryogenic cooling, low temperature operation

This work investigates the effects of temperature on the operation and performance of indium-phosphide (InP) based high-power broad-area laser (BAL) diodes operating in the eye-safe regime (1.5 μm – 2.0 μm). Low temperature (-80C to 0C) operation using a cryogenically cooled system enables investigation of temperature-dependent parameters such as threshold current, slope efficiency, diode voltage, and power conversion efficiency (PCE) of devices. Building upon established empirical models that describe threshold current and slope efficiency as functions of temperature, a key additional parametric model is developed to describe diode voltage incorporating a temperature dependence. With the inclusion of this temperature-dependent voltage model, the operational parameters are shown to accurately describe diode laser performance and enable simple prediction of PCE over a range of temperatures. Low-temperature-optimized 14xx nm devices with power conversion efficiencies greater than 50% at 5W and 19xx nm devices with PCE greater than 25% at 2W are characterized; results validate the developed temperature-dependent voltage model.

ACKNOWLEDGEMENTS

I would first like to express my sincerest gratitude to my thesis advisor, Dr. Paul Leisher, whose help and support were critical to the completion of my undergraduate and Master's degree. The past six years have been a defining period in my life; your guidance, both academically and professionally have been paramount in my development as an engineer and scholar. Life lessons, not necessarily expressed in your classroom but perhaps in your office or in simple conversation, are learned by many students who navigate Rose. You play a major role in shaping the lives of these students, and as I continue my educational journey, your lessons and advice will be at heart and mind.

To my committee members, Dr. Jeffery Leader and Dr. Richard Liptak (come visit Santa Barbara!): Thank you for your kind advice, revision suggestions, and generous assistance with my thesis completion. Your wise input added considerably to the content of this work – I am grateful for all that you have done to make my thesis a success.

To Dr. Azad Siahmakoun, Dean of Graduate Studies: Thank you for all of your help and assistance in the past months during the completion of my graduate degree. As I start my work at UCSB, I look forward to future chats with you about exciting research in silicon photonics and optical communications!

To Dr. Wonjong Joo: Thank you for all of your support during the wonderful study abroad adventure in Korea - my experiences at Seoul Tech and KIST were absolutely incredible! I will always be thankful for your boundless generosity – my fond memories of Korea will last a lifetime.

To Dr. Charles Joenathan: Six years ago, I sat in your Physics III classroom as a freshman mechanical engineering student; your passion for physics and optics piqued my curiosity for optical engineering. As I completed the process of switching majors (that same quarter!) and began the exciting journey down the optical engineering path, you were always available for help and support. Thank you for everything these past few years and for your pivotal role in my academic career!

To the Physics and Optical Engineering faculty – thank you for all of the incredible courses and for your absolute commitment to student success. Your passion for teaching instills in students a strong desire to succeed and pursue their own academic and career goals. The success of graduates is certainly a reflection of the unparalleled teaching environment here at Rose, made possible by dedicated, accomplished faculty.

To Pam Hamilton and Terri Gosnell, for your kind support which helped me to navigate Rose these past years and complete my undergraduate and graduate degrees.

To Roger Sladek, Ben Webster, and Brian Fair: The experimental results and labwork necessary for this thesis would not have been possible without your skilled expertise and support. I am very grateful for all of your help which was critical to the successful completion of my Master's degree.

And finally, to my parents, John and Leslie Brodnik: From a young age, you instilled in me a passion for learning and a strong curiosity, which have not faded as I have pursued my academic pursuits over the years. I would not be where I am today without your love and support which have made me the person I am.

And to any others not mentioned here, but certainly not forgotten: the completion of this thesis was made possible by an absolutely vast network of support here at Rose and abroad. I owe this work to the individuals in the background working to enable each and every student success.

Thank you all!

TABLE OF CONTENTS

LIST OF FIGURES

FIGURE **PAGE**

LIST OF TABLES

TABLE **PAGE**

LIST OF ABBREVIATIONS

DMM	Digital multimeter
DPSSL	Diode-pumped solid-state laser
E-k	Energy-momentum (Energy-wavevector) diagram
FCA	Free carrier absorption
IR	Infrared (electromagnetic wavelength 700nm – 1mm)
IVBA	Intervalence band absorption
LD	Laser diode
LED	Light emitting diode
LIV	Light – current – voltage (optical power, L [Watts] and diode voltage, V [Volts] vs. input current, I [Amps])
LN2	Liquid nitrogen
NIST	National Institute of Standards and Technology
OLS	Ordinary least squares regression
PCE	Power conversion efficiency (ratio of optical/electrical power)
SE	Slope efficiency - slope of *LI* curve: increase in optical power for a given increase in electrical power, units of Watts/Amp [W/A]
SRH	Shockley-Read-Hall non-radiative (‘trap-assisted’) recombination of carriers
TEC	Thermoeletric cooler
UV	Ultra-violet (electromagnetic wavelengths 10nm-400nm)
VI	Voltage, V [V] vs. current, I [A]
VT	Voltage, V [V] vs. temperature, T [K]
WLS	Weighted least squares regression

LIST OF SYMBOLS

A	cross sectional area of diode	m^2
α	absorption coefficient	m^{-1}
D_n, D_p	charge carrier diffusion coefficient (electron, hole)	cm^2/s
E_g	semiconductor energy bandgap	Joule [J]
η	slope efficiency	Watts per Amp [W/A]
g	gain coefficient	m^{-1}
g_{th}	threshold gain	m^{-1}
h	Planck's constant	Js
I	diode current	Amperes [A]
I_s	reverse bias saturation current	A
I_{th}	threshold current	A
J	current density	A/m^2
k	Boltzmann constant	1.38e-23 J/K
L	optical power ('light')	Watts [W]
L_n, L_p	diffusion length (electron, hole)	m
M	empirical voltage-temperature parameter	mV/K
m_n^*, m_p^*	effective mass (electron, hole)	kg
m_0	free electron mass	kg
n	denotes negative charge carrier (electron)	
N_c, N_v	effective density of states (conduction band, valence band)	$1/cm^3$
N_d, N_a	donor concentration, acceptor concentration	$1/cm^3$

n_i	intrinsic carrier density	$1/cm^3$
p	denotes positive charge carrier (hole)	
q	fundamental electron charge	1.602e-19 Coulombs [C]
R	reflectance	[0 to 1]
R_s	series resistance	ohms [Ω]
T	temperature	Kelvin [K]
T_0	threshold current model temperature parameter	K
T_1	slope efficiency model temperature parameter	K
V	diode voltage	Volts [V]
V_0	zero voltage (i.e. ‘turn-on’ voltage, or forward voltage)	V
V_T	thermal voltage	V

1.0 INTRODUCTION

1.1 Introduction to laser diodes

Laser diodes (LDs) are electrically pumped semiconductor devices that generate coherent laser light via stimulated recombination of charge carriers (electron-hole pairs). There are numerous application advantages of semiconductor laser devices:

- Low-cost [1]
- Small footprint and packaging options (**Figure 1.1**)
- Efficient, stable operation over long lifetimes (>10,000 hours) [2]
- Wide range of wavelengths available - UV to mid-infrared [3]
- Wide range of output powers – tens of milliwatts to tens of watts for single emitters (highly scalable operation with high-power, multi-diode arrays achieving kilowatt operation) [3]

Figure 1.1 C-mount style single emitter diode laser (left) and sample multi-diode array and fiber-coupled packages (right) [4]

Possessing these desirable qualities, laser diodes are the most common laser device [5] used in a wide host of applications in consumer, industrial, medical, military, and academic

markets [6]. Low power (tens of milliwatts) laser diodes are commonly used in consumer electronics such as DVD/Blu-ray players, barcode readers, and laser range finders. Single mode LDs are used in the telecommunication industry as data transmitters in fiber optic links. High-power diode stacks are used in industrial material processing (e.g. laser welding), medical and surgical operations, remote sensing and spectroscopy, and military and directed energy applications [3].

Particular interest in the development of efficiency-optimized diode lasers has been expressed by the high-energy physics community for use as optical pump sources in high-power laser systems. Solid-state and fiber-based laser systems are the current state-of-the-art (laser) technologies in accelerator applications that range from electron beam creation and control to plasma-based particle generation [3]. Rare-earth-ion doped crystal and fiber (Erbium, 1.5-1.6 μm and Thulium, 1.7-2.1 μm) are common gain media employed in such laser systems. Boasting high-power scalability, wide range of wavelength capabilities in the near IR for resonant pumping schemes [9], and high power conversion efficiencies, diode laser arrays are ideal optical pump sources for solid state and fiber lasers.

These systems require careful thermal management of gain media due to the high average powers associated with high repetition-rate, high peak-power operation [10]. Excess heat generated in the gain media due to high-power pump sources is necessarily extracted via heat sinks and cooling systems. Thus, refrigeration systems are often present in particle accelerator applications that incorporate especially-high power solid-state or fiber laser sources. Current state-of-the-art cooling technologies for efficient operation use cryogenic liquid coolants (e.g. liquid nitrogen at 77K). In applications that require active refrigeration of gain media, extension of the cooling system to the diode pump sources is one potential method to increase total system

efficiency by improving electrical-to-optical conversion efficiency of the diode pump sources. Targeted design of these pump diodes specifically for operation at low temperature (as opposed to cooling room-temperature-optimized diodes) can further improve system efficiency [9, 10].

1.2 **Principle of operation**

Semiconductor laser diodes are forward-biased PN junction devices that generate photons from radiative recombination of charge carriers [8]. They differ from light-emitting-diodes (LEDs) – also PN junction devices – in that the dominant photon generation mechanism is stimulated emission, where LEDs operate on spontaneous emission. To achieve stimulated emission, positive feedback of photons is made possible via a Fabry-Perot resonant cavity made by parallel cleaved facets of the semiconductor gain medium [8]. Shown in **Figure 1.2** is a sample structure of a laser diode device labelled with p- and n-type regions and metal contacts for power supply.

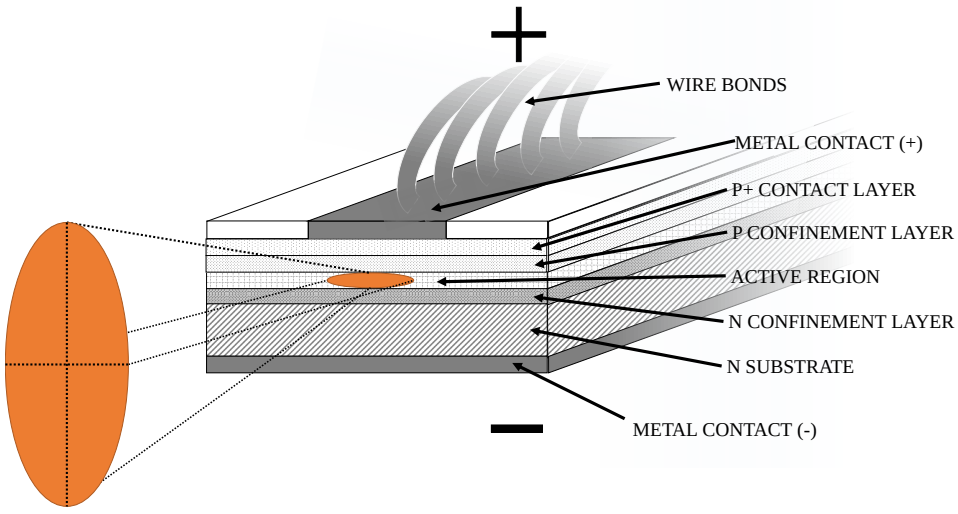

Figure 1.2 Schematic diagram of sample double heterostructure laser diode. Current flows from top to bottom, through the active region where radiative recombination occurs.

Electrical current flows across the PN junction during operation, increasing the charge carrier density (electron-hole pairs) in the depletion region thus increasing radiative and non-radiative recombination. As electron-hole pairs recombine to generate photons, spontaneous emission (isotropic, incoherent) first dominates the radiative recombination rate over stimulated emission (directional, coherent laser output). At a sufficiently high injection current level (defined below in Eq. 1.6), stimulated emission becomes the primary photon generation mechanism. This occurs after cavity losses – spontaneous emission (photons emitted into unwanted optical output), absorption, scattering, and mirror losses – are compensated via sufficient photon generation, and loss is equal to the cavity gain. A brief accounting of photon loss vs. photon gain for a simple diode laser cavity is provided in **Figure 1.3** to demonstrate this effect.

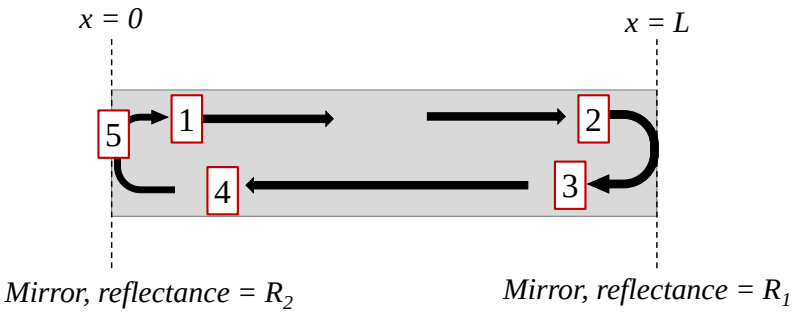

Figure 1.3 **Schematic of a laser diode with cavity length, *L*, to aid in demonstration of intensity considerations for round trip optical gain and loss**

At 1: directed to the right	$I(x = 0^+) = I_0$	1.1
At 2: directed to the right	$I(x = L^-) = I_0 e^{(g-\alpha)L}$	1.2
At 3: directed to the left	$I(x = L^-) = R_1 \cdot I_0 e^{(g-\alpha)L}$	1.3
At 4: directed to the left	$I(x = 0^+) = R_1 \cdot I_0 e^{(g-\alpha)2L}$	1.4
At 5: directed to the right	$I(x = 0^+) = R_1 R_2 \cdot I_0 e^{(g-\alpha)2L}$	1.5

In Eqs. (1.1-1.5) above, g and α correspond to gain and loss coefficients (respectively), R_1 and R_2 correspond to mirror reflectivities, and L is the cavity length [11]. For lasing to occur,

round trip intensity, I, must be equal to the initial intensity, I_0 [11]. Substituting $I(x)=I_0$ (for a roundtrip $x=2L$) into Eq. (1.5) and solving for g yields the gain at which stimulated emission surpasses spontaneous emission, defined as the threshold gain, g_{th}.

$$g_{th} = \alpha + \frac{1}{2L} ln\left(\frac{1}{R_1 R_2}\right) \qquad 1.6$$

This 'turn on' condition (onset of stimulated emission output over spontaneous emission) is defined as the lasing threshold for the device [8]. The relationship of output power vs. drive current for the two previously described operation regimes – spontaneous emission when current is below threshold and stimulated emission (lasing action) beyond threshold – is shown in **Figure 1.4** below.

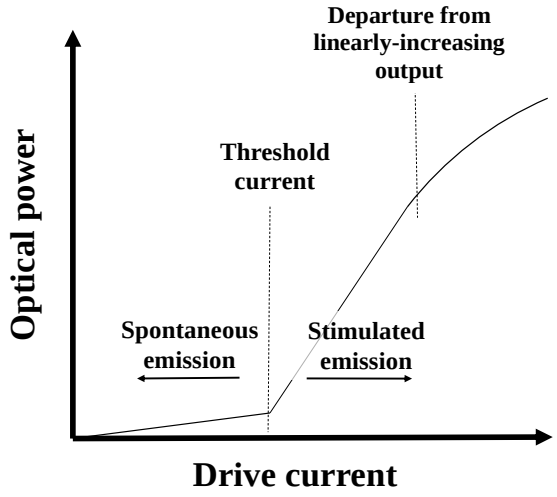

Figure 1.4 Spontaneous and stimulated emission operation regimes for a laser diode. At high current, self-heating leads to decreased operation efficiency and departure from linearly increasing output power

Being electrically pumped semiconductor devices, temperature-dependent charge carrier dynamics must be considered in addition to photon dynamics to fully describe diode laser operation (a thorough temperature-dependent analysis of a forward biased PN junction diode is included in **Section 4.0**). Generally speaking, unwanted non-radiative recombination increases

with temperature, leading to less efficient conversion of injected carriers to photons and a decrease in laser efficiency. This occurs because g_{th} is constant with temperature (to first order); as temperature increases, carrier density and energies increase as predicted by Fermi-Dirac statistics [12]. The thermal increase of carrier energies to levels above the lasing level leads to a decrease in laser gain, $g(n)$; the carrier density required to reach threshold gain ($g(n) = g_{th}$) and to achieve stimulated emission is therefore elevated at higher temperatures, requiring an increase in injected current for laser operation. Energetic carriers relax by giving energy to lattice vibrations (phonons) further increasing junction temperature. Thermal management of diode lasers, especially at high power and injection levels (to mitigate temperature increase due to self-heating via nonradiative recombination and phonon generation), is therefore critical for maintaining optimum power conversion efficiencies of laser systems. To this end, efforts are made to carefully design and incorporate both passive and active cooling systems (**Figure 1.5**) in laser diode applications.

Figure 1.5 Example of a passive (left) metal-fin heat sink for TO can style laser diode [13]. Active (right) refrigeration system for liquid coolant circulation [14].

Additionally, specific design of low temperature devices to maximize benefits of cooling systems and minimize heat generation can improve total system performance. Research endeavors

in both the scientific and industrial communities aim to develop a deeper understanding of these temperature effects on laser diode operation to advance design for low temperature diode laser applications.

2.0 MOTIVATION

Common metrics used to quantitatively describe laser diode performance are optical power and power conversion efficiency (PCE) as functions of drive current. To describe optical-power, L (Watts, or W), as a function of current, I (Amps, or A), it is necessary to know the injection level at which the laser turns on and the conversion efficiency of injected carriers to photons of useful laser output. These two operation parameters that describe turn-on current and conversion efficiency of photons from injected carriers are defined as threshold current, I_{th}, and slope efficiency, η, respectively. If threshold current and slope efficiency are known, then optical power as a function of drive current can be estimated; the slope and intercept of a linear approximation of L vs. I sufficiently describes operation for low currents (before self-heating causes departure from linearly increasing output power), shown in **Figure 2.1**.

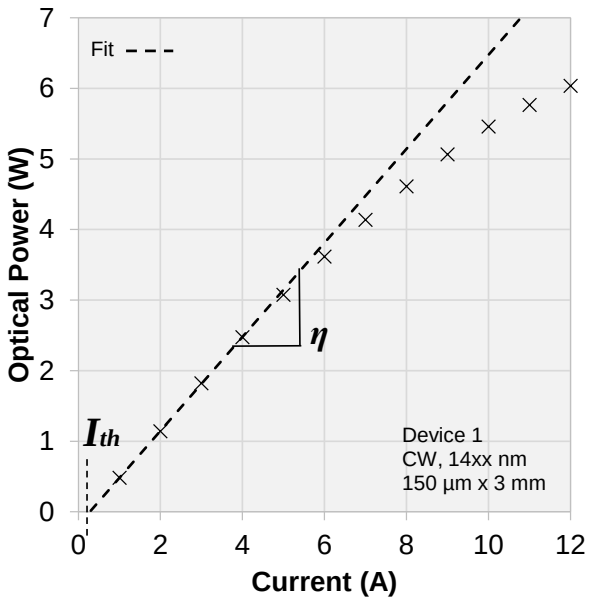

Figure 2.1 Laboratory LI data approximated by a least squares linear fit (to linear region, 1-4A) via parameters I_{th} and η.

The complete physical picture that describes these operation parameters is complex. Carrier dynamics for a PN junction diode coupled with photon dynamics for a Fabry-Perot laser resonator must be analyzed to fully illustrate diode laser operation. In most scenarios, however, the full physical picture is not necessary for implementation. A handful of relevant metrics and plots are sufficient: optical power, L, and voltage, V, as a function of current, I, provide what is known as the diode LIV curve. With this information known, power conversion efficiency (sometimes called 'wallplug' efficiency) is also known. Input electrical power and PCE are found via Eq. (2.1) and Eq. (2.2) using the LIV data.

$$Electrical\ power, P = Voltage \cdot Current = V \cdot I \tag{2.1}$$

$$Power\ conversion\ efficiency\ (PCE) = \frac{Optical\ power}{Electrical\ power} = \frac{L}{V \cdot I} \tag{2.2}$$

However, an LIV curve accurately describes the operation at a single operation temperature only. Changes in temperature due to heat generated during operation or cooling via heat management systems affects the optical and electrical characteristics of the diode laser device. To account for temperature-dependent effects when describing diode performance, one could experimentally measure LIV curves for every desired operation temperature. This has the clear disadvantage of being a time- and resource-intensive endeavor. Alternatively, key components of the LIV curves could be parametrically modelled as a function of temperature, allowing approximation of LIV data for an arbitrary temperature input over a defined range. Two of these key components are the previously mentioned threshold current, I_{th}, and slope efficiency, η.

Simple empirical models have been established based on experimental characterization of diode laser operation versus temperature to predict changes in threshold current and slope

efficiency for a given temperature change, ΔT. These models, described in further detail in **Section 4**, depend on several parameters that are found experimentally for a given device. After the relevant parameters are defined for the device, optical output power as a function of current (the LI curve) is known for a range of operation temperatures. Importantly, these models do not require a complex analysis of the physics of operation: several empirical terms are sufficient for predicting performance.

However, a critical piece of the LIV and PCE empirical description is missing: without knowledge of the voltage behavior as a function of temperature and current, it is not possible to model power conversion efficiency of the device to fully predict performance. The aim of this work is to investigate diode voltage versus current over a range of temperatures and to develop a suitable empirical model to describe voltage-temperature behavior. This voltage-temperature model will complete the LIV and PCE picture, enabling a full description of relevant operation parameters.

3.0 LITERATURE REVIEW AND RELATED RESEARCH

Development of high-efficiency semiconductor laser design improvements requires an understanding of temperature-dependent diode laser phenomena. The previously described operational parameters used to characterize diode performance (threshold current (I_{th}), slope efficiency (η), and diode voltage (V)) exhibit temperature dependencies governed by charge carrier dynamics and optical loss mechanisms described in the following sections. Experiments conducted to determine the dominant loss mechanisms relevant to each operational parameter offer insight into targeted design approaches; namely, efforts to minimize threshold current and diode voltage and maximize slope efficiency [15-17]. Recognizing the benefits of operating room-temperature-optimized devices at low temperatures, incorporation of cryogenic cooling systems have yielded ultra-high power, high-efficiency diode laser devices [10, 19]. Furthermore, advancement of design approaches for diode lasers designated specifically for low-temperature operation have aided development of long-wavelength laser diodes with power conversion efficiencies exceeding 75% [9, 10].

3.1 Laser threshold vs. temperature

Carrier losses are caused by non-radiative recombination events such as Auger and Shockley-Reed-Hall (SRH) recombination (**Figure 3.1**), radiative loss due to spontaneous emission (not into useful output), and carrier leakage from charge carriers escaping the active region [12].

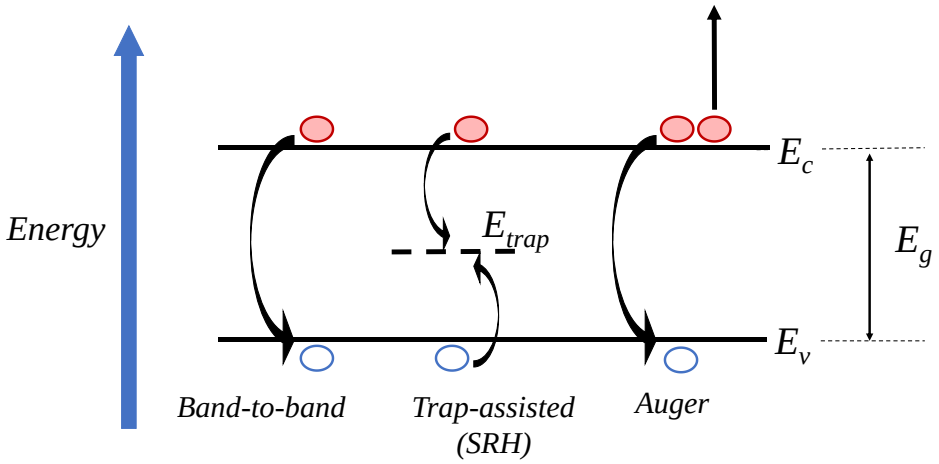

Figure 3.1 Non-radiative loss mechanisms for diode lasers

Shockley-Reed-Hall recombination, sometimes referred to as trap-assisted recombination, occurs when an energy level between the conduction and valence band (trap) becomes temporarily occupied by an electron which then further relaxes to the valence band via annihilation with a hole. The trap energy level which enables the two-step recombination process to occur is a result of a foreign atom or defect in the semiconductor crystal lattice. Auger recombination, a three-body event (therefore having a probability that is dependent on carrier density cubed), is a non-radiative recombination process where an electron relaxes to a valence band hole, transferring its energy to a previously excited conduction band electron. The Auger recombination coefficient displays an Arrhenius-type dependence on temperature [16]; i.e. there is an 'activation energy' below which the effect is insignificant. At lower temperatures, the cubic dependence on carrier density (which decreases according to Fermi-Dirac statistics) combined with the reduction in the Auger recombination coefficient results in a negligible contribution to carrier loss. The overall result is a considerable decrease in threshold current for laser diodes when temperature is decreased [18].

For long wavelength devices discussed in this work (eye-safe regime), the dominant temperature-dependent carrier loss mechanism is Auger recombination [17]. A single Auger recombination event results in the loss of an electron-hole pair (necessary for stimulated emission of a photon), loss of a third (now highly energetic) electron from the active region, and heat generation as the third electron relaxes via phonon creation and lattice vibrations. This resulting increase in temperature leads to an increase in carrier density and Auger coefficient, further increasing the non-radiative recombination rates and decreasing the efficiency of the diode device.

3.2 **Slope efficiency vs. temperature**

Intrinsic optical losses decrease with decreasing temperature, manifesting as an increase in slope efficiency, η. Optical losses include scattering and absorption within the device and losses at each cleaved facet, dependent on surface ('mirror') reflectances. Mirror losses and scattering due to lattice defects do not vary much with temperature [2]. Free carrier absorption (FCA) and intervalence band absorption (IVBA) are generally agreed to be the primary absorption mechanisms contributing to optical loss of long wavelength devices [20, 21]. FCA occurs when a free electron in the conduction band absorbs a photon and is elevated to a higher energy level. The excited electron then de-excites via phonon generation, increasing the temperature of the system. IVBA is a free-carrier-absorption-type process in which a valence band hole is triggered by a photon and transitions to another energy level within the valence band. Shown in **Figure 3.2** is an energy-wavevector (E-k) diagram demonstrating the IVBA process where a heavy hole (higher effective mass) transitions to a light hole (lower effective mass) band after receiving energy from an absorbed photon.

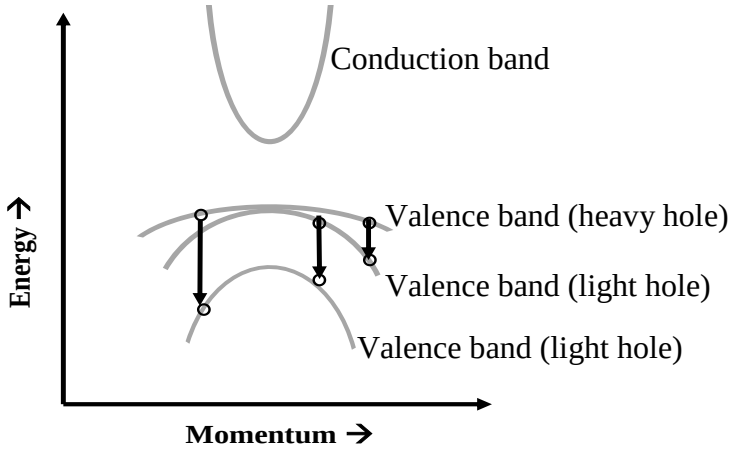

Figure 3.2 E-k diagram demonstrating various intervalence band absorption transtions from heavy-hole to light-hole bands

IVBA decreases with decreasing temperatures due to carrier-density dependent gain, *g(n)*, remaining constant with temperature; at lower temperatures, fewer carriers are necessary to satisfy the threshold gain condition. This decrease in IVBA photon absorption (with *g* constant) corresponds to an increase in slope efficiency since a larger portion of injected carriers contribute to laser output. As such, cooling devices to low temperatures is an effective means to increase slope efficiency and performance of a laser diode.

3.3 Diode voltage vs. temperature

The diode voltage required to maintain a given input current increases with decreasing temperature due to a decrease in the thermal energy contribution to charge carriers. In other words, a decrease in thermionic emission (temperature-driven flow of sufficiently energetic charge carriers) at low temperatures necessitates a higher bias voltage for carriers to overcome potential barriers (material heterobarriers and defects) to enable current flow. Additionally, low temperature operation leads to freeze-out of holes, further increasing voltage required for operation [22].

Experimental data (**Figure 3.3** *VI* curve for several temperatures and **Figure 3.4** *VT* fit) demonstrate an approximately linear decrease in voltage with increasing temperature.

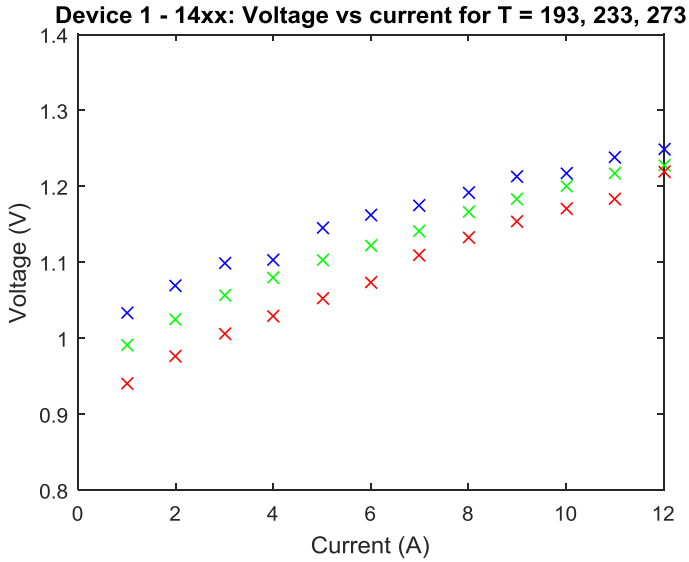

Figure 3.3 **Sample experimental *VI* data for several operation temperatures. Device 1: 14xx nm. (top to bottom: 193K, 233K, 273K)**

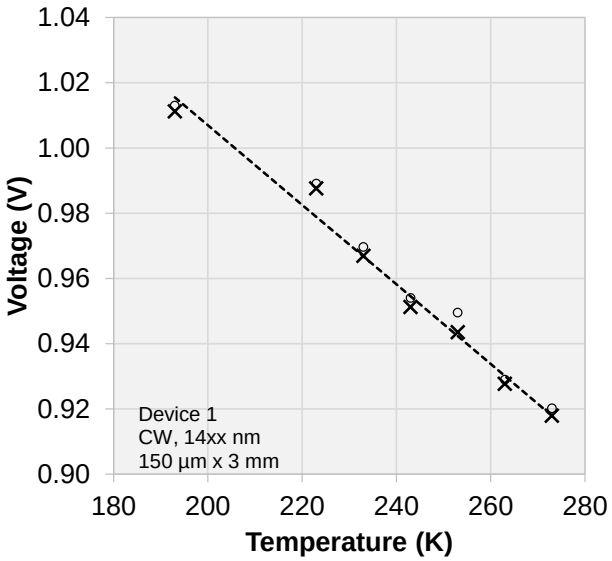

Figure 3.4 **Diode voltage decreases linearly with temperature**

This voltage effect decreases device performance as temperature is decreased, directly competing with the improvements in threshold current and slope efficiency at low temperatures. Therefore, at a certain temperature the benefits of further cooling are no longer realizable; the decrease in efficiency due to higher diode voltage surpasses the benefits of decreased threshold current and increased slope efficiency. A thorough understanding of the temperature-dependent voltage characteristics is therefore critical for optimizing diode laser performance. Development of the empirical voltage model in this work will simplify voltage description of semiconductor laser devices and facilitate further design improvements for low temperature devices.

4.0 DESCRIPTION OF THE MODEL

4.1 Empirical models for diode laser operation

Threshold current and slope efficiency vary with junction temperature, T (Kelvin, or K). Simple models that are used to predict changes in threshold current, I_{th} (A, or Amps) and slope efficiency, η (W/A, or Watts per Amp) as temperature varies are shown below [23]:

$$I_{th} = I_{th,ref}\, exp\left(\frac{\Delta T}{T_0}\right) \quad 4.1$$

$$\eta = \eta_{ref}\, exp\left(-\frac{\Delta T}{T_1}\right) \quad 4.2$$

Here, T_0 and T_1 are empirical parameters for a typical laser diode that quantitatively describe a particular device's sensitivity to a change in junction temperature, $\Delta T = T_j - T_{j,ref}$ (compared to each parameter at reference temperature, typically 20 or 25°C, for $I_{th,ref}$ a η_{ref}), of threshold current (T_0) and slope efficiency (T_1). The practicality of these models lies in the fact that they describe laser output as a function of temperature using a single parameter each for threshold current and slope efficiency and avoid complex analysis of the underlying physics. Thus, temperature-dependent optical power output characteristics (light, or L) for a given device are known once T_0 and T_1 are determined – slope and intercept for each operation temperature are defined, resulting in a linear output power as a function of current (LI) model.

4.2 Threshold current: I_{TH} and T_0

In **Figure 4.1**, experimental data for test diodes 'Device 1: 14xx nm' and 'Device 2: 19xx nm' with parametric model fits for threshold current versus temperature are shown.

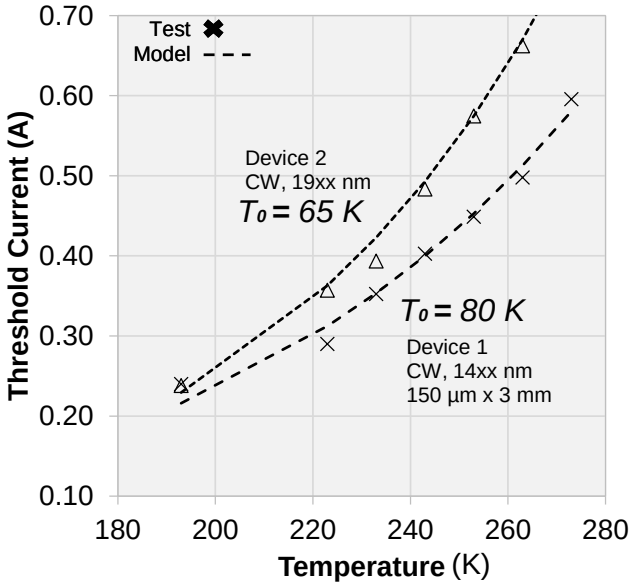

Figure 4.1 Sample of parametric fit using T_0 to model threshold current as a function of temperature.

A larger T_0 describes a device with a lower threshold current sensitivity to temperature. A value of T_0 = *infinity* would describe a device that exhibits no change in threshold current as temperature is varied while a T_0 value near zero (but not equal to zero) describes a rapidly (near vertical) increasing threshold current as temperature is increased.

4.3 Slope efficiency: η and T_1

Slope efficiency, η (W/A), modeled using Eq. (4.2) with temperature parameter T_1, characterizes the conversion efficiency of injected charge carriers to photons of laser light. A slope efficiency of 100% describes operation where an increase in input electrical power results in an equivalent increase in output optical power, i.e. linear slope is equal to 1 W/A. Real devices do not exhibit this ideal behavior and have conversion efficiencies less than 100% stemming from the

loss mechanisms related to carrier energy, carrier density, photon energy, and photon density previously described in **Section 2**.

4.4 Current-voltage behavior of a PN diode

The voltage and current behavior for a laser diode can be effectively described using simple PN junction diode relations starting with the ideal diode model shown below [12].

$$I(V) = I_s(e^{\frac{qV}{kT}} - 1) \tag{4.3}$$

The current across the diode *I(V)* depends on the reverse bias saturation current, I_s, temperature, *T*, and voltage, *V*. In this first order approximation, saturation current and voltage are assumed to constant with temperature. The *q/kT* term in the exponential is rewritten as the thermal voltage, V_T, for convenience:

$$V_T(T) = \frac{kT}{q} \tag{4.4}$$

Note that above in Eq. (4.4) the temperature dependence on thermal voltage is explicitly stated by denoting $V_T(T)$. The *IV* relation is more accurately described as additional terms are allowed to vary with *T*. When these terms are 'freed up' to change with T, they will be identified via function notation *f(T)*. This progressive improvement in current-voltage approximation accuracy will be demonstrated in the following sections by incrementally incorporating temperature dependence for relevant parameters (summarized in **Table 4.1** on page 43).

The current-voltage (*IV*) relationship is now rewritten as a voltage-current (*VI*) relationship to conform to real-world operation of diodes. Since carrier injection levels are what primarily

define photon generation rate, diode lasers are controlled via current sources. It is therefore more convenient to view the *VI* relationship with current as the independent term and to calculate the diode voltage for various injection levels and temperatures.

$$V(I,T) = V_T(T) \cdot ln\left(\frac{I}{I_s} - 1\right) + I \cdot R_s \qquad 4.5$$

Again, for this first order model all parameters (with the exception of thermal voltage, *V(T)*) are assumed constant with temperature. Shown below in **Figure 4.2** is this first order V-I relationship:

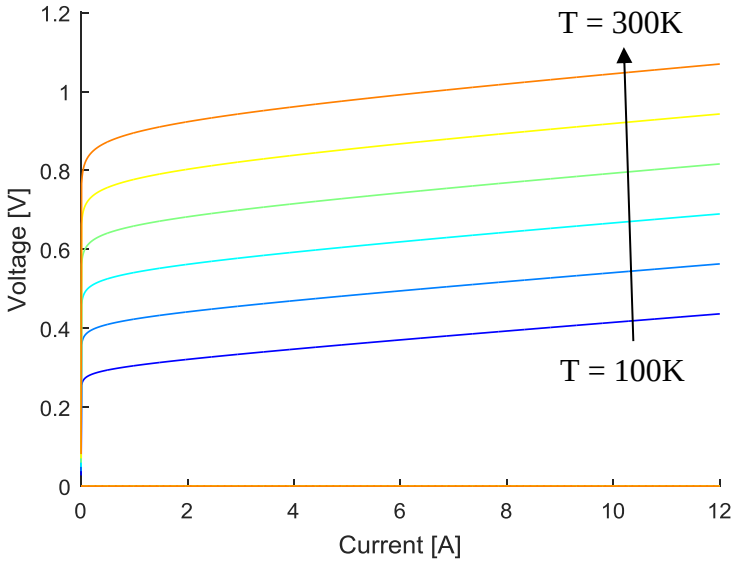

Figure 4.2 First order V-I relationship for various temperatures. Bottom to top: T = 100, 140, 180, 220, 260, and 300 K.

The above plot shows the 1st order voltage-current relationship for a range of temperatures between 100 and 300K. Important to note is that the lowermost curve (T = 100K) displays a lower operation voltage than the higher temperature curves. This is the opposite of what is expected and what has been previously demonstrated with experimental data in **Figure 3.3**: a higher junction temperature should result in an increased thermal energy contribution to the charge carriers, and

therefore reduce the total required supply bias voltage for a given injection level. In a real laser diode, diode voltage decreases with increasing temperature (refer back to **Figure 3.4)**. **Figure 4.3** below highlights the issues with the 1st order approximation: it is unrealistic to assume reverse saturation current, I_s, and intrinsic carrier density, n_i, are constant with temperature.

(A)

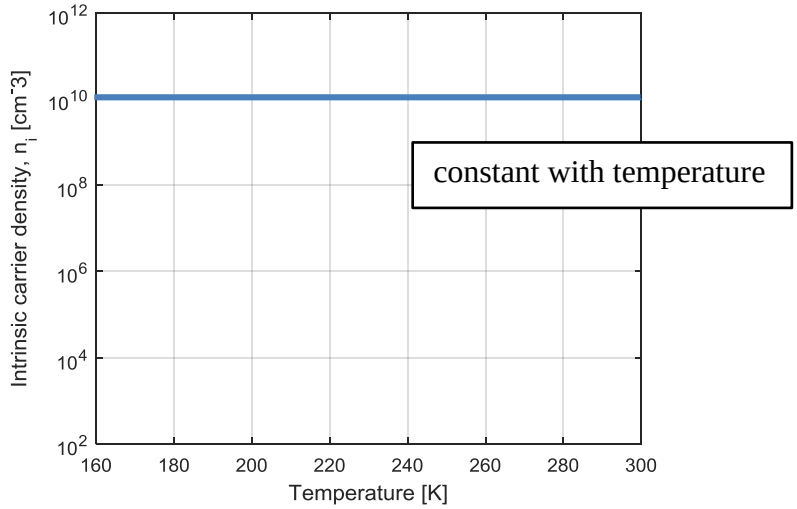

(B)

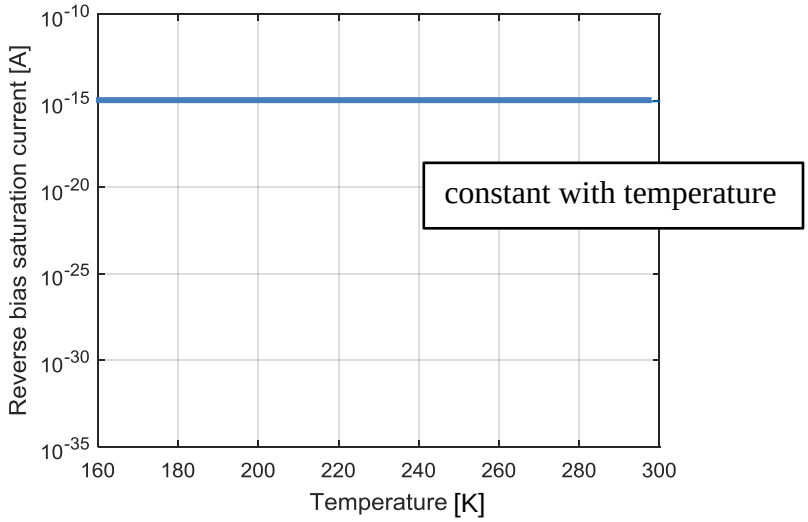

Figure 4.3 (A) Intrinsic carrier concentration and (B) reverse bias saturation current. 1st order approximation, constant over temperature

In this first order approximation, the major issue (and resulting V-I description issues) is due to the assumption that reverse bias saturation current does not vary with temperature. A more accurate approximation defines I_s in the following manner [12]:

$$I_s(T) = Aq\left[\frac{D_p}{N_D L_p} + \frac{D_n}{N_A L_n}\right] \cdot n_i^2(T) \qquad 4.6$$

where *A* is the cross sectional area of the device (to describe current through the device, *I*, instead of current density, *J*), *D* (subscripted *p* and *n* for *p-type* and *n-type* regions) is the carrier diffusivity, *N* (subscripted *D* for *donor* and *A* for *acceptor*) is the donor and acceptor concentration, and *L* is the diffusion length. The intrinsic carrier concentration n_i varies with temperature in this second order approximation as well:

$$n_i^2(T) = N_c N_v \cdot e^{-\frac{E_g}{kT}} \qquad 4.7$$

where N_c and N_v denote carrier concentration in the conduction and valence bands, respectively. The material bandgap, E_g, defined as the difference in the conduction band and valence band energy levels, varies with temperature as well; for this second order approximation it is assumed to be constant. In **Figure 4.4** the intrinsic carrier concentration and reverse bias saturation current are shown as functions of temperature for both the 1st order (constant with temperature) and 2nd order (partial temperature dependence) cases.

(A)

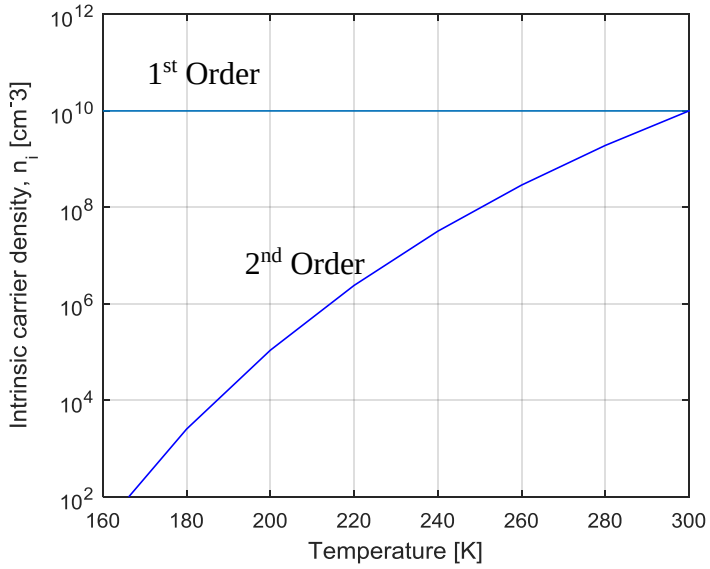

(B)

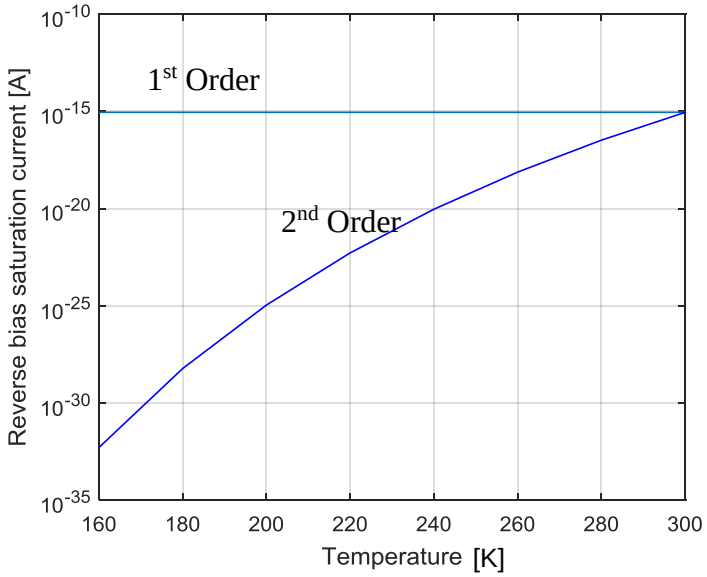

Figure 4.4 Intrinsic carrier density (A) and reverse bias saturation current (B), 1st and 2nd order.

An intrinsic carrier density evaluated at 300K for the first order case differs from the second order case by over 5 orders of magnitude at T = 160K. This results in a disparity in reverse bias saturation current of more than 10 orders of magnitude at T=160K between the 1st and 2nd

order evaluations. The 2nd order V-I relationship, a function of temperature in $V(T)$, $I_s(T)$, and $n_i^2(T)$, is shown in **Figure 4.5** on the following page.

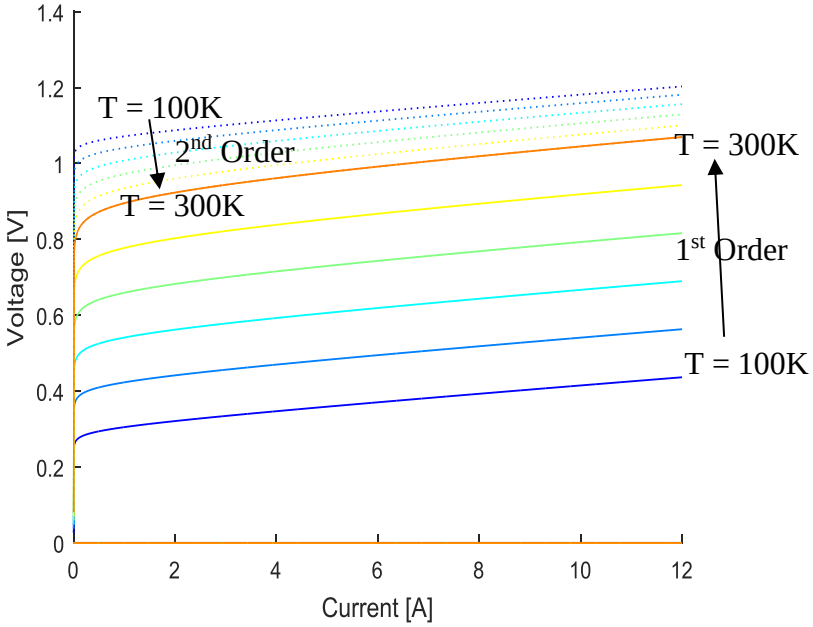

Figure 4.5 Voltage-current (V-I) relation for various temperatures, T = 100 to 300 K. Shown is the 2nd order (dotted) alongside the 1st order (solid) evaluations.

Note that in the 2nd order approximation, operation voltages decrease as temperature increases. This is what is expected during diode operation, validating the increase in model accuracy as temperature dependence of additional terms is incorporated.

For the 3rd order model, all terms that exhibit temperature dependence are allowed to vary with T:

$$n_i^2(T) = N_c(T)N_v(T)e^{-\frac{E_g(T)}{2kT}} = 2\left(\frac{2\pi k}{h^2}\right)^{\frac{3}{2}}\left[\left(\frac{m_n^*(T)}{m_0}\right)\left(\frac{m_p^*(T)}{m_0}\right)\right]^{\frac{3}{4}} \cdot T^{\frac{3}{2}} \cdot e^{-\frac{E_g(T)}{2kT}} \qquad 4.8$$

In Eq. (4.8) above, m^* (subscripted n and p for electrons and holes, respectively) denotes the effective mass of charge carriers as a function of temperature. An approximation of the weak

temperature dependence of the electron and hole effective masses employed in the 3rd order model is provided below via a polynomial fit.

$$\frac{m_n^*}{m_0} = A_n + B_n T - C_n T^2 \tag{4.9}$$

$$\frac{m_p^*}{m_0} = A_p + B_p T - C_p T^2 \tag{4.10}$$

where *A, B, C* (subscripted with *n*- and *p*- carriers) are fit parameters following the analysis by Barber et. al. [24]. The bandgap, E_g, is also now modelled with temperature dependence via the parametric fit shown below, with fit parameters *a* and *b* [25]:

$$E_g = E_{g0} - \frac{aT^2}{T+b} \tag{4.11}$$

Using the equation above, a sample semiconductor (Silicon) bandgap temperature dependence $E_g(T)$ is shown in **Figure 4.6**. The bandgap varies by approximately 0.04 eV between temperatures T = 100K and T = 300K in this example.

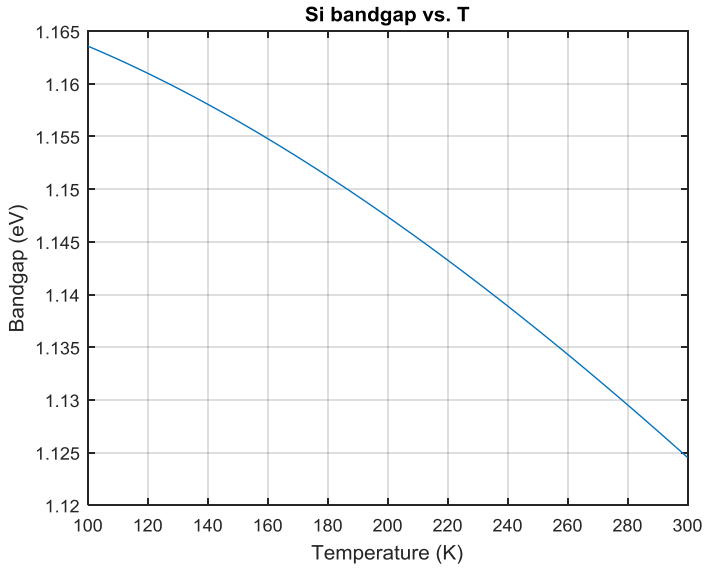

Figure 4.6 Sample of semiconductor material (Si in this example) bandgap variation versus temperature, $E_g(T)$ for T = 100K→300K.

The 3rd order intrinsic carrier concentration and reverse bias saturation currents (which incorporate temperature dependence for all previously described terms) are compared to the 2nd order approximation in **Figure 4.7** below.

(A)

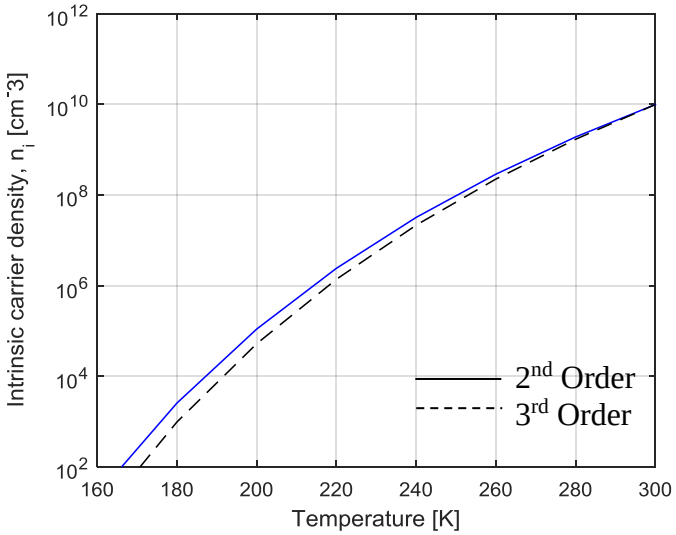

(B)

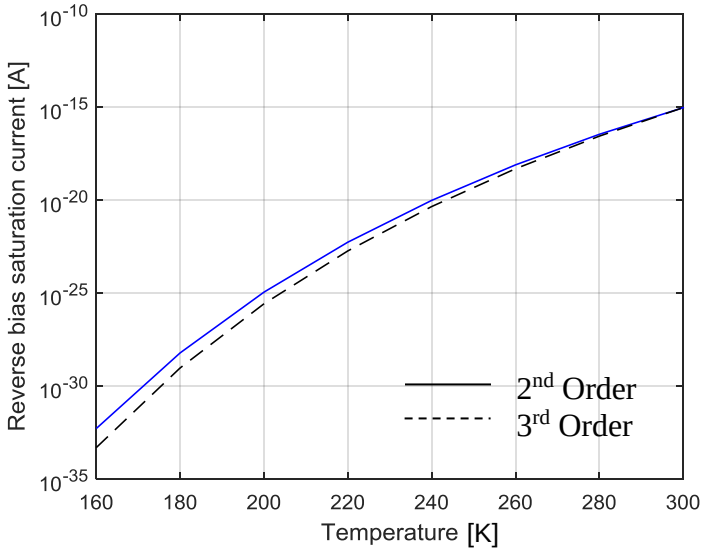

Figure 4.7 Intrinsic carrier concentration (A) and reverse bias current (B) vs. temperature for 2nd and 3rd order models

Parameters that include temperature dependence in the 3rd (and not 2nd) have little impact on *VI* relation. 1st, 2nd, and 3rd order approximations are rewritten below to clarify the progression of the ***VI(T)*** model as full temperature dependence of relevant terms is incrementally incorporated:

Table 4.1 Summary of ideal diode equation as additional terms incorporate temperature dependency

1st	$V(I,T) = V_T(T) \cdot ln\left(\frac{I}{I_s} - 1\right) + I \cdot R_s$ $V_T(T) \to \frac{kT}{q}\ , \qquad I_s = const.$
2nd	$V(I,T) = V_T(T) \cdot \ln\left(\frac{I}{I_s(T)} - 1\right) + I \cdot R_s$ $I_s(T) \to\ Aq\left[\frac{D_p}{N_D L_p} + \frac{D_n}{N_A L_n}\right] \cdot n_i^2(T)$ $n_i^2(T) \to N_c N_v \cdot e^{-\frac{E_g}{kT}}\ \ , \quad E_g = const.$
3rd	$V(I,T) = V_T(T) \cdot ln\left(\frac{I}{Aq\left[\frac{D_p}{N_D L_p} + \frac{D_n}{N_A L_n}\right] \cdot N_c(T) N_v(T) \cdot e^{-\frac{E_g(T)}{kT}}} - 1\right) + IR_s$ $N_c(T) N_v(T) \cdot e^{-\frac{E_g(T)}{kT}} \to 2\left(\frac{2\pi k}{h^2}\right)^{\frac{3}{2}}\left[\left(\frac{m_n^*(T)}{m_0}\right)\left(\frac{m_p^*(T)}{m_0}\right)\right]^{\frac{3}{4}} \cdot T^{\frac{3}{2}} \cdot e^{-\frac{E_g(T)}{2kT}}$ $\frac{m_n^*}{m_0} \to A_n + B_n T - C_n T^2$ $\frac{m_p^*}{m_0} \to A_p + B_p T - C_p T^2$ $E_g(T) \to E_{g0} - \frac{aT^2}{T+b}$

The increase in model accuracy for the 3rd order evaluation which incorporates temperature dependence for all relevant terms is demonstrated in **Figure 4.8** below. Note that the 2nd and 3rd order evaluations are equivalent at T=300K; this is as expected, since the 2nd order terms which are assumed constant are evaluated at T=300K, resulting in identical approximations at this operating temperature.

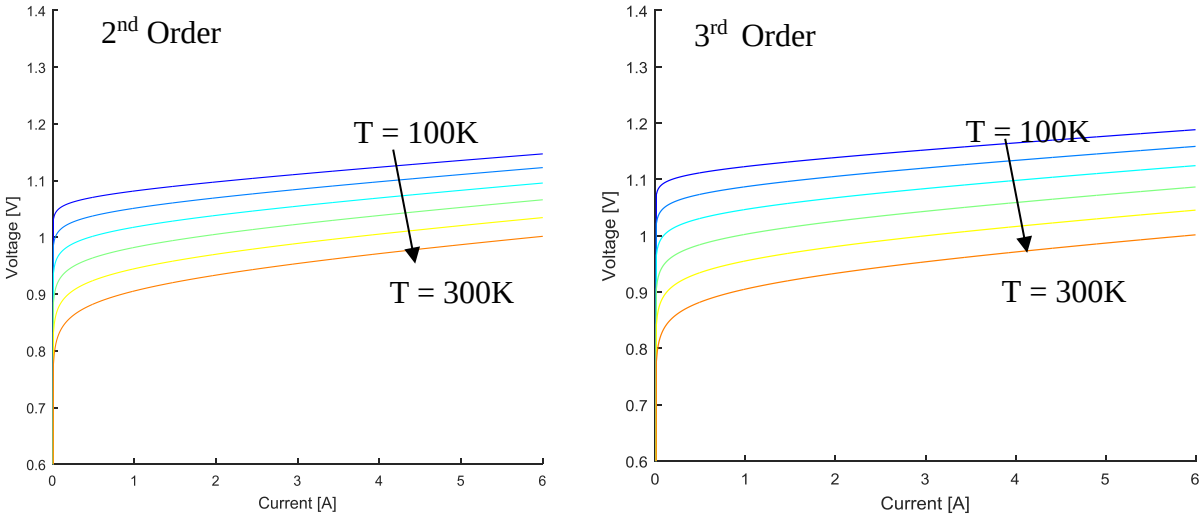

Figure 4.8 2nd (left) and 3rd (right) order VI characteristic curves. Temperatures 100-300K

Examining the 2nd and 3rd order approximations side-by-side, the increased accuracy as a consequence of the full temperature dependence is apparent; the diode voltage, *V*, at all currents, *I*, is roughly 5% greater in the 3rd order evaluation compared to the 2nd order at the lowest temperature T = 100K. This result is better understood by analyzing the change in voltage as a function of temperature, evaluated at a given injection current. This is equivalent to evaluating the

diode voltage of each temperature curve along a vertical line that corresponds to the operation current, shown in **Figure 4.9** below and plotted in **Figure 4.10**.

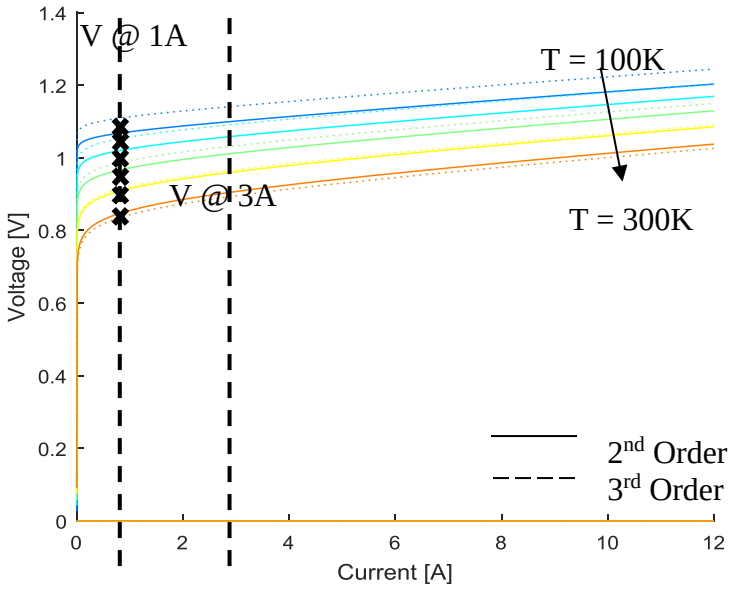

Figure 4.9 **Representation of voltage vs. temperature evaluation for operating currents I = 1 and 3 Amps.**

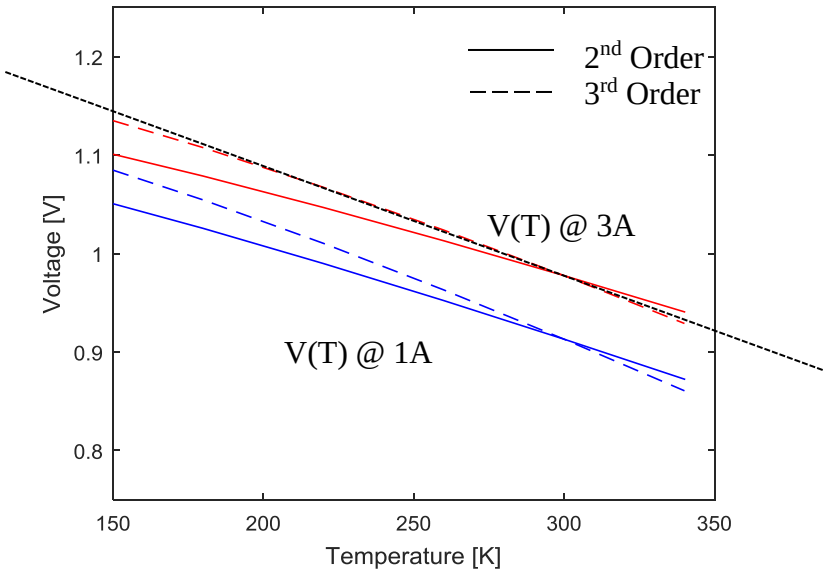

Figure 4.10 ***V(T)* sample plot for 1A and 3A operating currents. Shown are 2nd (solid) and 3rd (dash) order evaluations. Behavior is approximated with a linear trend (dotted)**

In **Figure 4.10**, 2nd and 3rd order *V(T)* evaluations are plotted; the voltage varies approximately linearly with temperature. By describing the voltage versus temperature relationship as a simple linear trend (found experimentally, similar to threshold current parameter, T_0, and slope efficiency parameter, T_1), the analysis of the current-voltage characteristics previously described can be avoided while adequately modelling device operation: the complex temperature-dependent behavior of the 3rd order *V(T)* model is bundled into a single device parameter.

The proposed parametric model for voltage as a function of temperature for a laser diode is defined and experimentally determined as follows:

- ➔ A single parameter, ***M*** having units **[mV/K]**, corresponds to $\Delta V_0/\Delta T$ (slope of the line approximating $V_0(T)$); see **Fig. 13** and the following definition of V_0

1. To experimentally determine *M*, measure the diode voltage as a function of injection current (*VI* curve) for a range of operation temperatures
2. Fit a line to the *VI* curve in the range beyond turn-on (note that the slope of this line is the series resistance of the device, R_s) for each temperature
3. Record the y-intercept (for convenience will now be called ***V_0*, the 'zero-voltage'**) of this line for each operation temperature
4. This single curve, $V_0(T)$, can now be described with the defined *M*-parameter, corresponding to the slope of the linear approximation

Provided this newly defined voltage-temperature parameter, *M*, and the series resistance, R_s (effectively temperature-independent) of a laser diode, the change in voltage as a function of

temperature and current is adequately and simplistically described. Coupled with the established T_0 and T_1 (threshold current and slope efficiency) parametric models, the *M*-parameter allows for a more thorough description of device performance by enabling prediction of power conversion efficiency (PCE) as a function of temperature. Validation of this newly presented parametric model with agreement to experimental data is provided in **Section 6.0**

5.0 METHODS

5.1 Overview

Low temperature testing of laser diodes required development of an environmentally controllable test bench. At the low temperatures (less than -50°C) desired for temperature-dependent characterization of test devices, condensation of moisture and impurities onto cold surfaces is an issue. Condensation of water vapor and other gases present in air at atmospheric conditions onto the diode facet affects operation and can result in contamination and damage of test device. An appropriate test setup for consistent and stable temperature tests down to at least -80°C (193K) should therefore incorporate humidity and environmental control. Convenient optical and electrical access are necessary to measure diode LIV characteristics. Several test solutions were considered and evaluated prior to implementation of the final diode characterization setup.

Table 5.1 Overview of potential testing stations for low temperature diode laser characterization

Environmental chamber	Tabletop enclosure	Vacuum-cryostat
Cold-cycle environmental chamber for low temperature (233K) device testing (no humidity control)	Thermoelectric cooler + chiller combination cold test stage with plastic enclosure for inert gas flow (humidity mitigation)	Commercial liquid-nitrogen-cooled optical device testing unit. Vacuum station removes atmosphere and prevents condensation issues

5.1.1 Windowed refrigerator environmental test chamber

A refrigerant-cooled test chamber capable of temperature control down to -40°C was considered as an option for the diode test bench. Optical access to the test device was possible through a viewing window on the front of the unit. A small side port with a thermally-isolating

foam plug permits electrical connections for current supply and voltage measurement at the diode. Limitations of the refrigerator unit test setup included lack of humidity control and ill-defined optical losses through the multi-pane viewing window. To mitigate condensation issues associated with poor humidity control of the test chamber, inert gas could be flowed through the chamber to replace atmospheric air and eliminate moisture. This, in addition to construction of an entirely custom diode fixture within the chamber greatly increased the complexity of the test procedure. Poor thermal contact of the diode mount with the chamber (convective only, built on posts in the chamber) limits the heatsinking capabilities of the setup resulting in increased operation temperature of the heatsink and diode junction.

5.1.2 Custom tabletop environmental test chamber

Construction of a custom, environmentally-controllable test setup on an optical table was explored as an alternative to the refrigeration unit. A liquid cooled (water + ethylene glycol) copper heatsink in combination with a thermoelectric cooler (TEC) could be used to achieve low temperature diode testing. A chiller running a 50/50 ethylene glycol/water mixture can effectively cool a copper block heatsink to temperatures near 0°C. A thermoelectric cooler driven with an appropriate temperature controller can maintain a temperature differential between the 'hot' and 'cold' faces of the TEC device. By sinking heat from the TEC 'hot' face through the cooled copper block, the TEC can be driven to maintain a lower temperature on the cold face. The performance of the chiller and TEC combination was investigated; lab tests struggled to achieve temperatures below -20°C.

The construction of this setup on a lab bench top additionally suffered from direct exposure to atmosphere. Similar to the refrigeration chamber, condensation of moisture onto the diode facet

becomes an issue at low temperatures. To eliminate moisture from the test environment, nitrogen gas could be flowed into an enclosed test setup. To this end, a plastic enclosure could be used to contain the controlled gas environment or a custom chamber could be constructed around the test setup. Both options increase the complexity of the test setup and affect the repeatability of the test procedure.

5.1.3 Cryostat + vacuum pump

The third test setup considered incorporates a liquid nitrogen (LN2) cooled cryostat (Oxford Optistat DN-V) and vacuum pumping station. Optical cryostats are specifically designed for laboratory experiments such as spectroscopy that require low temperatures or cold detectors (down to ~77K for liquid nitrogen, ~4K for liquid helium). Vacuum pressures below ~$1x10^{-4}$ Torr are necessary for adequate convective thermal isolation of the cold-arm from surrounding atmosphere. Additionally, removal of the air from the test chamber eliminates the issue of moisture condensation onto the test devices. At sufficiently low vacuum pressures, however, backstreaming of oil from wet pumps becomes an issue. Oil that is streamed into the chamber condenses onto cold surfaces of the cryostat – in the case of the cryostat, these surfaces are the LN2 vessel and cold arm with the mounted test device. A vacuum system for operation with the cryostat should therefore be fully dry. A turbomolecular pump backed by a (dry) diaphragm pump (Pfeiffer HiCube Eco80 pumping station) capable of pumping to less than 1e-4 Torr was purchased as an appropriate solution.

The cryostat unit was shipped with a submount for industry standard C-mount diode laser devices (**Figure 5.1**– C-mount devices). In-house fabrication of an aluminum mount for chip-on-submount (**Figure 5.2** and **Figure 5.3**) single-emitter testing achieved efficient thermal contact of

the heatsink with the cold arm of the cryostat and enabled easy swapping of custom submount test devices. Electrical access for the diode current supply and voltage probes was possible through a vacuum sealed electrical port on the top of the cryostat.

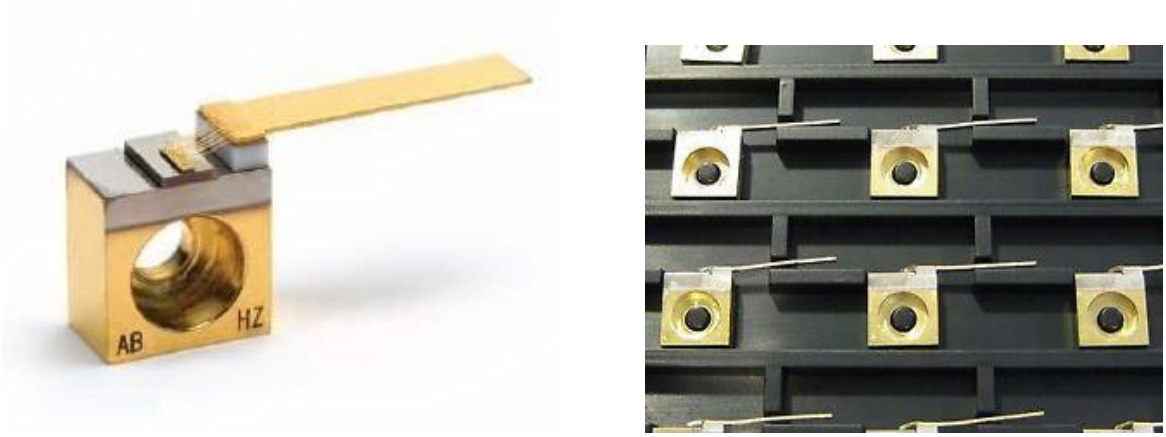

Figure 5.1 **Left: Single C-mount laser diode, showing gold wire bonds to metal contact flag. Right: Tray of several C-mount laser diode devices for low-temperature performance characterization.**

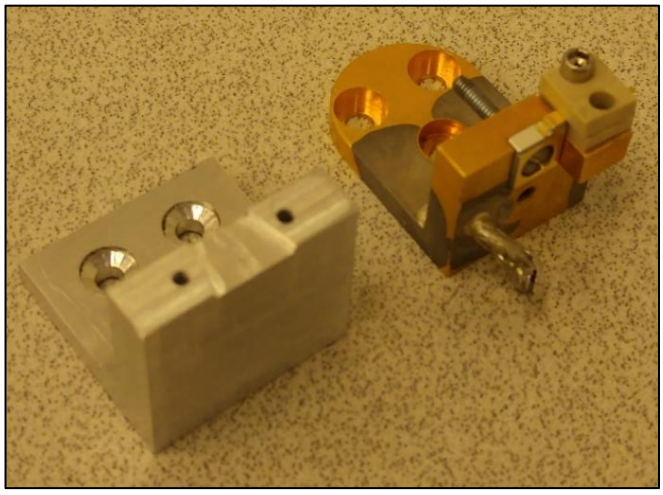

Figure 5.2 **Submount designed and fabricated in-house (left) for simple positioning of test devices onto the cold arm of the cryostat. Diode current supply and voltage measurement provided by soldered leads**

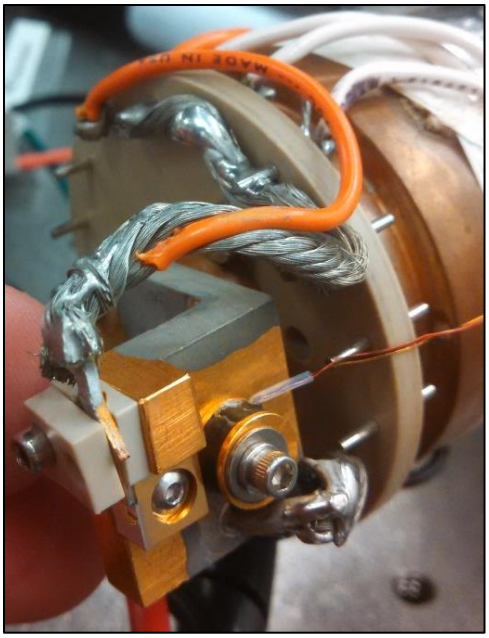

Figure 5.3 Submount fixed to cold arm of cryostat. Diode current supply and voltage measurement provided by wires soldered through electrical isolator and fixed to mount via screws.

An integrated temperature controller (Mercury ITC) allowed consistent, stable temperature set points of the test device in the cryostat by balancing the flow of liquid nitrogen to the cold arm and integrated heater control. Regulation of both the heatsink temperature (77K to >300K) and testing environment coupled with simple electrical and optical access resulted in a convenient, highly repeatable testing station for device characterization at low temperatures.

As a tool to aid in the down-selection of potential test setups, a decision matrix was constructed and is shown (**Table 5.2**). Testing solutions were evaluated in four categories: complexity, cost, control, and repeatability. Higher scores reflect more desirable traits of each test setup - the setup with the highest score was chosen as the final test solution.

Table 5.2 Decision matrix for down-selection of test setup. Each option is scored 1-5, with higher scores being more desirable. Highest total score (Cryostat+vacuum: 15) is selected as the final test setup.

	Refrigeration chamber	Tabletop chamber	Cryostat + vacuum
Complexity	2	1	4
Cost	4	5	1
Control	2	1	5
Repeatability	3	2	5
TOTAL	**11**	**9**	**15**

High complexity inherent to the refrigerator and tabletop chamber arises from the need to construct entirely custom test setups and to flow inert gas to mitigate condensation issues. These issues for the refrigerator and tabletop setup are reflected in the low scores for complexity and control, while the cryostat scores highly here due to the convenience of the environmentally-controllable laboratory package. The cryostat scores lowest in the cost category due to the high cost of the lab equipment and necessity of a pumping station and temperature controller. The high level of repeatability and precise temperature/environmental control necessary for device characterization outweigh the high cost associated with the cryostat, however, and the cryo/vacuum system was chosen for laboratory tests.

The cryostat setup proved to be an appropriate solution that allowed simple, precise temperature measurements of diode devices (**Figure 5.4 - Figure 5.6**). Operation under vacuum mitigated the issue of condensation of moisture onto devices which could result in poor operation and device damage. The fully dry pumping station (**Figure 5.7**) eliminated the risk of oil backstreamed into the chamber which could affect diode performance.

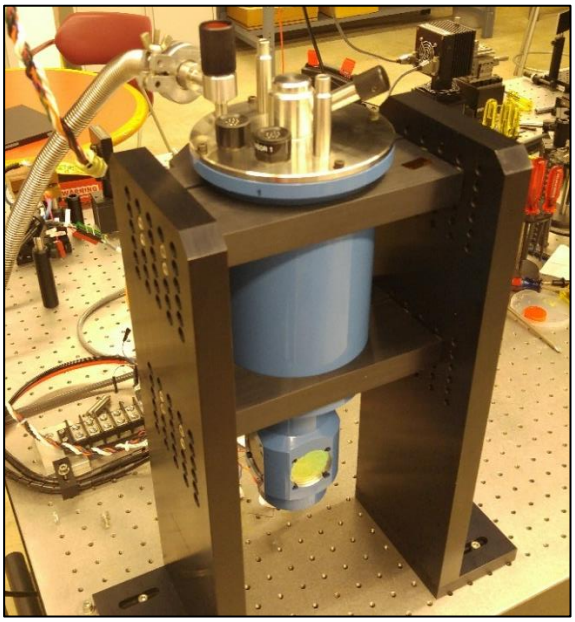

Figure 5.4 **Optistat DN-V cryostat chamber for low temperature device testing. Top chamber houses the liquid nitrogen in thermally isolated dewar, with vent-controlled flow to cold arm in bottom chamber**

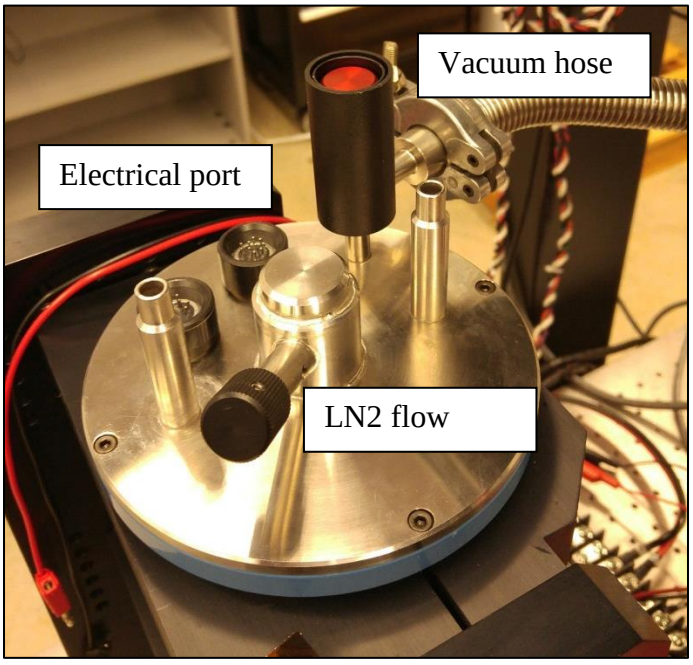

Figure 5.5 **Top view of cryostat. Vacuum hose connection, LN2 flow control, electrical access to test devices.**

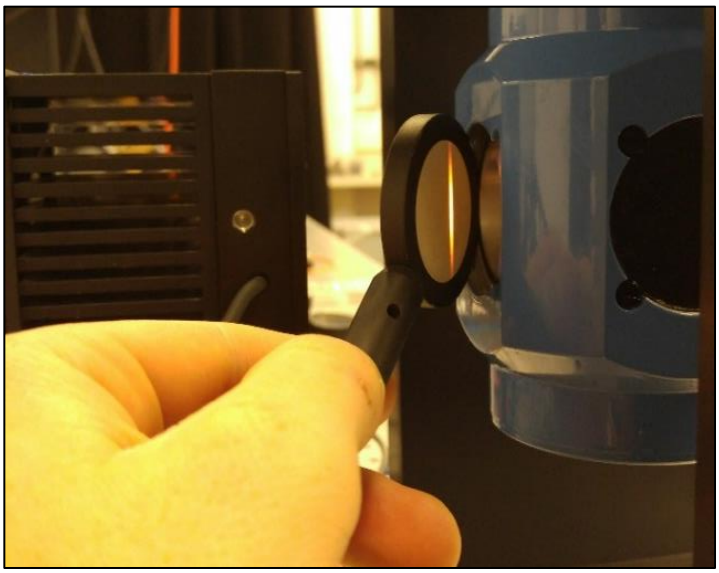

Figure 5.6 **Laser viewed on IR phosphor wand through window of cryostat.**

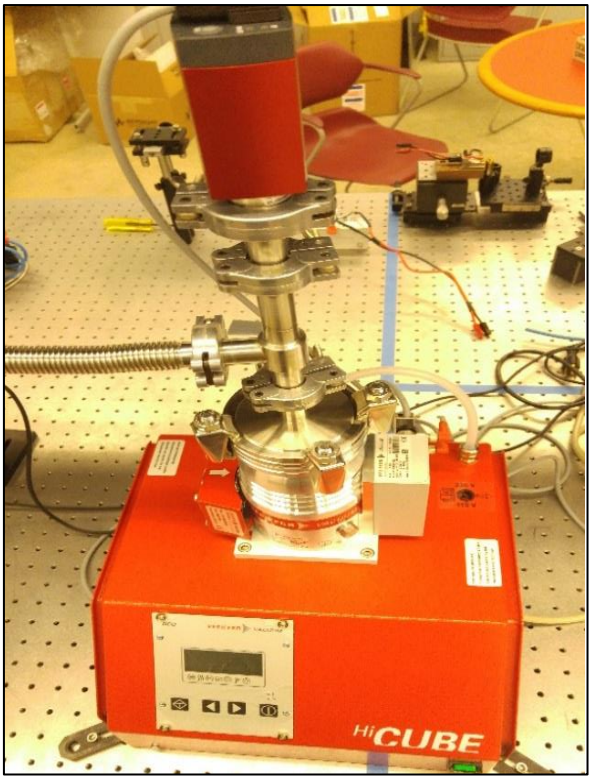

Figure 5.7 **Pfieffer HiCube ECO80 turbomolecular pumping station, necessary for low-temperature cryostat operation.**

5.2 Diode performance measurement methods

LIV characteristics for each test device were measured using the vacuum-cryostat system described above. A calibrated high-power, air-cooled thermopile (Gentec-EO, NIST-traceable) was used to measure optical power of the laser as a function of drive current. Thermopiles are an array of thermocouples which generate a thermoelectric current from temperature gradients. A thermopile power meter converts the associated change in temperature due to heating caused by absorbed radiation into a measurement of optical power. With an appropriate material to absorb incident radiation, thermopiles are ideal sensors for IR measurements due to relatively flat absorption (and therefore measurement sensitivity) over the wavelength range. Diode voltage was measured using a digital multimeter (DMM) with probes fed through the cryostat chamber to the chip. Each test device was characterized between 193K and 298K (-80°C to 25°C).

Table 5.3 Equipment list for vacuum-cryostat characterization station

DEVICE / MODEL	MANUFACTURER
Optistat DN-V (optical cryostat)	Oxford Scientific
HiCube ECO80 turbomolelular vacuum pump	Pfeiffer Vacuum
Digital multimeter (Fluke series 80)	Fluke
High-power thermopile (power meter)	Gentec EO
Optical spectrum analyzer (AQ6730D)	Yokogawa

5.3 'Gold standard' test setup

Calibration of the measured voltage and optical power was necessary to correct for series resistance effects of the high current and voltage probe wires fed into the chamber and for optical power loss due to clipping of the fast axis and reflectance losses of the cryostat window. A

calibration setup was built on the lab table to perform voltage and optical power experiments to be defined as ‘gold standard’ measurements.

For the chip-on-submount devices, a four-point-probe setup was used to collect the gold standard calibration data (**Figure 5.8**). Voltage was probed directly at the diode and the thermopile was positioned at the emitter to accurately measure optical power. For the C-mount devices, a thermoelectric cooled diode laser mount (Arroyo, series 242 laser mount) was used to perform LIV tabletop calibration experiments (**Figure 5.9**). Voltage was measured via probe wires built into the mount; optical power was measured using the thermopile positioned at the emitter. Data was collected at room temperature and defined as the gold standard for each test device. Each device was then characterized in the cryostat setup at the same temperature setpoint as the gold standard TEC laser mount experiment.

The voltage increase with drive current due to series resistance was assumed to be equal at each temperature setpoint (summarized in following section). The optical losses due to clipping and window reflectance through the cryostat port were assumed to be constant over the wavelength range tested for each device. Thus, the temperature-dependent wavelength shift for each device over the tested temperature range was assumed to result in a negligible change in optical loss for each device. The gold standard test point (room temperature, 298K) was used to calibrate the voltage and optical loss for every temperature setpoint. Optical losses and series resistance effects inherent to the test setup accounted for 5~10% decrease in measured wallplug efficiency of tested devices.

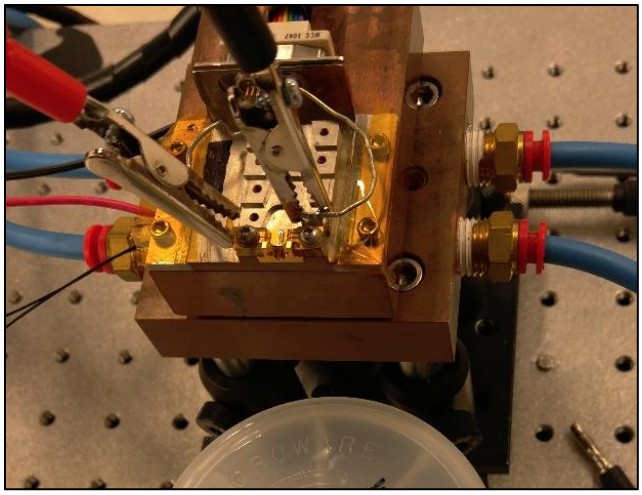

Figure 5.8 **Gold standard test setup for submount test devices. Voltage measured directly at the laser diode. Thermistor and TEC were used for precision temperature control. Optical power was measured with a high-power thermopile.**

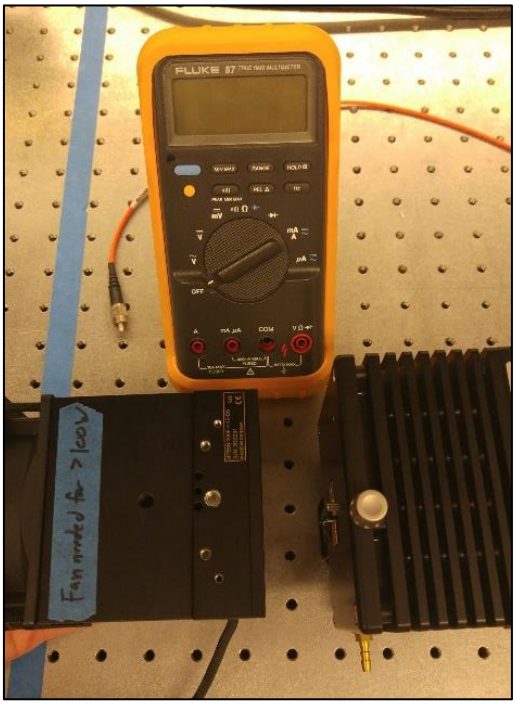

Figure 5.9 **Gold standard test setup for C-mount test devices. Voltage measured directly at the laser diode via wires to Arroyo mount. Optical power was measured with a high-power thermopile.**

6.0 RESULTS

6.1 Description of data

Experimental data and characterization for a single laser diode are summarized in the following sections to demonstrate the analysis method. The characterization process for each test device is identical (results for each device are provided in **Appendix A**).

Using the previously described vacuum-cryostat setup, LIV data for each chip was collected at various temperatures between 150K and 300K. First, a calibration using the gold standard setup at room temperature was conducted. A sample comparison of the voltage and optical power measured using the gold standard setup and the cryostat is provided in **Figure 6.1** and **Figure 6.2**. The difference in measured voltage (due to series resistance of wire leads used for current supply) is subtracted out for the voltage measurements at each temperature for each device (**Figure 6.1**).

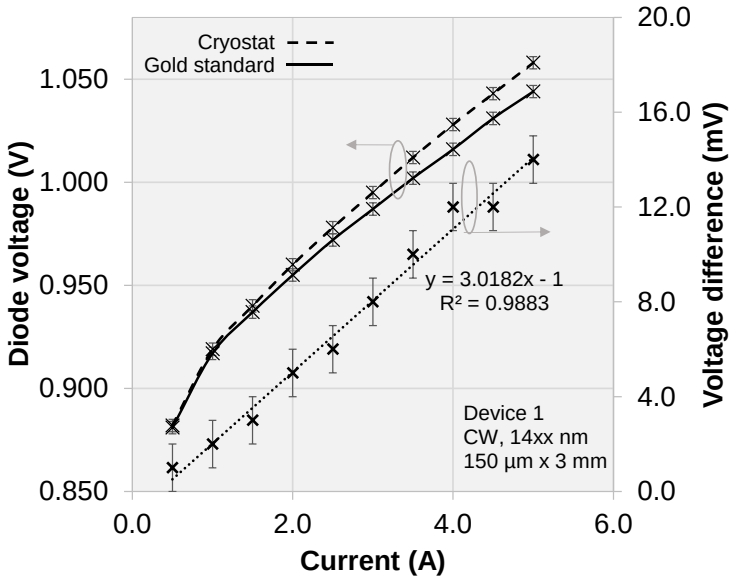

Figure 6.1 Voltage calibration using gold standard setup and cryostat measurements at room temperature

Optical power loss due to beam clipping and window reflectance (experimentally found to account for between 5-10% power loss) is next accounted for; this sample calibration is shown in **Figure 6.2**.

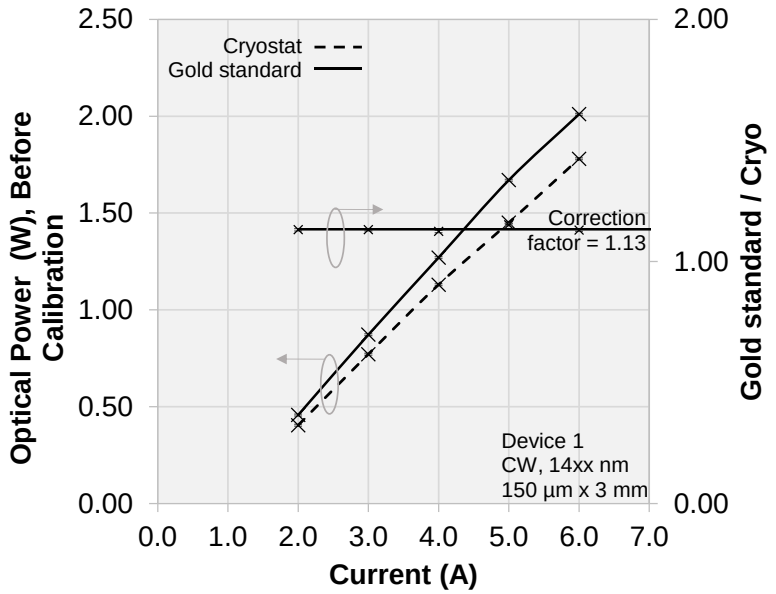

Figure 6.2 Optical power calibration using gold standard and cryostat measurements at room temperature.

After determining the calibration factors for voltage and optical measurements, LIV data was collected. A sample room temperature LIV measurement demonstrating gold standard calibration is provided in **Figure 6.3** on the following page.

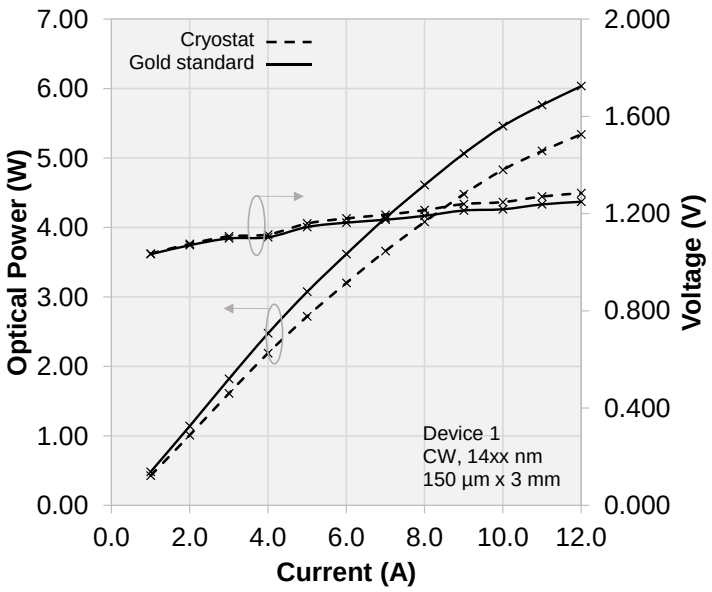

Figure 6.3 Sample of room temperature LIV curve before and after calibration of series resistance and optical losses

The calibration factors for the room temperature test are applied for each temperature set point – series resistance and clipping losses are assumed to vary a negligible amount with temperature. This assumption is reasonable – changes in series resistance effects are inherent to the changes in bulk semiconductor conductivity which varies an insignificant amount over the tested temperature range. Additional changes in series resistance can be attributed to changes in conductivity of wire leads. A temperature-dependent change in conductivity due to cryogenic cooling would only affect components in thermal contact with the cold arm; the wire leads outside of the cryostat are unaffected by the changes in operation temperature and therefore the resistance of the entire link varies a negligible amount for the temperature tests (experimental data in **Figure 6.8** justifies the series resistance insensitivity to temperature – the slopes of the *VI* curves provided do not change with temperature). Optical power losses due to clipping and, primarily, window reflectance are also assumed constant with temperature. Temperature-dependent wavelength drift

for each device assumed to be 0.5 nm/°C equates to a change in wavelength of 50nm over the tested temperature range of 190-300K; manufacturer specification for the wavelength-dependent reflectivity of the C-coated cryostat window (provided in **Appendix B**) is flat over the wavelength range of tested devices.

LIV curves for 'Device 1: 14xx nm' over the tested temperature range (193K to 298K) are shown in **Figure 6.4** below. The optical output increases linearly at low drive currents (slope of this line is the previously defined slope efficiency, η), but begins to roll over due to self-heating at higher currents.

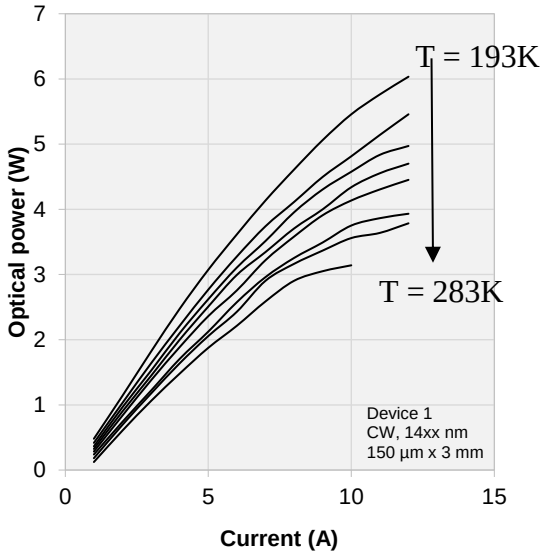

Figure 6.4 Sample Light vs. Current (LI) curve set for temperature tests (193K, 223K, 233K, 243K, 253K, 263K, 273K, 283K) for 'Device 1: 14xx nm'.

From the *LI* curves shown above, threshold current and slope efficiency parameters (T_0 and T_1) can be extracted. **Figure 6.5** and **Figure 6.6** demonstrate sample least squares regression fits to linear portions of the *LI* and *VI* curves for a single temperature. The linear range (before power-rollover due to self-heating) for the *LI* curves is defined between 1 and 4 amps.

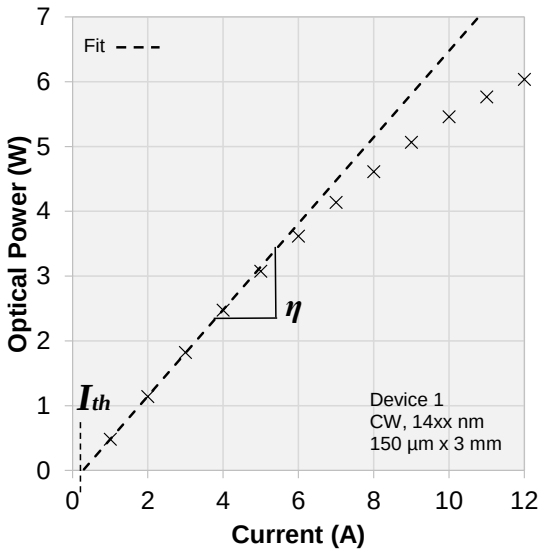

Figure 6.5 Least squares fit to linear range (1 to 4A) *LI* curve for threshold current I_{th} and slope efficiency η determination for a single temperature

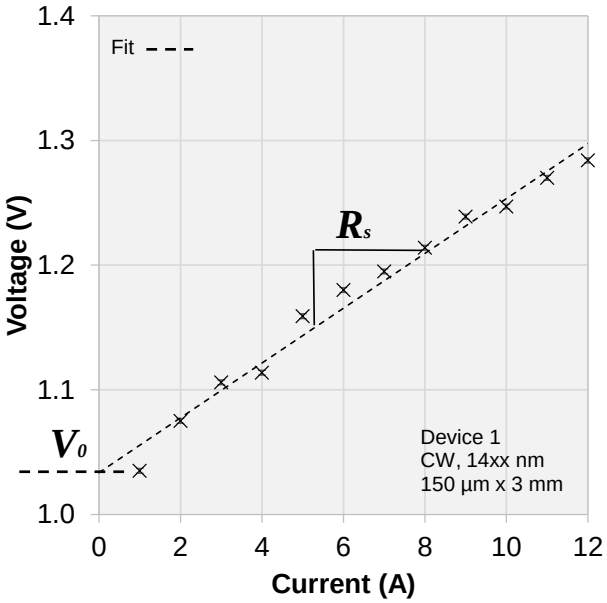

Figure 6.6 Linear fit to *VI* curve for series resitance (R_s, slope) and V_0 (y-intercept) determination for a single temperature

The previously described linear fits to light-current and voltage-current curves are implemented at every temperature set point to generate the desired temperature-dependent-

parameter curves $I_{th}(T)$, $\eta(T)$, and $V_0(T)$ corresponding to threshold current, slope efficiency, and 'zero voltage,' respectively. Temperature-insensitive series resistance, R_s, is found by averaging all R_s values determined by the slope of each linear *VI* fit. Shown in **Figure 6.7**and **Figure 6.8** are sample *LI* and *VI* curve sets for every tested temperature of a particular device ('Device 1: 14xx nm') demonstrating the full evaluation process for parameter calculations.

For the measured *LI* curves shown in **Figure 6.7**, a multiplicative error of 1.5% is associated with each optical power measurement due to the measurement uncertainty of the thermopile; ordinary least squares regression routines are robust and accommodate this multiplicative error.

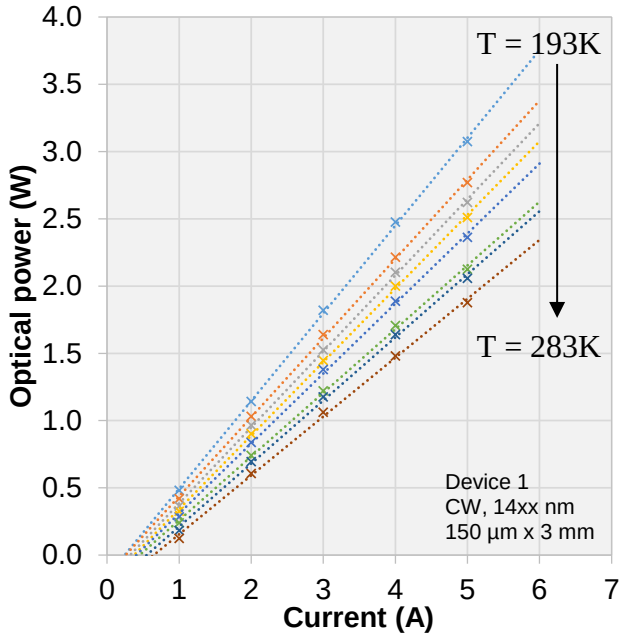

Figure 6.7 **Linear region of each LI curve at every tested temperatures. X-intercept of each linear fit is the threshold current of the device. Top to bottom: 193K, 223K, 233K, 243K, 253K, 263K, 273K, 283K**

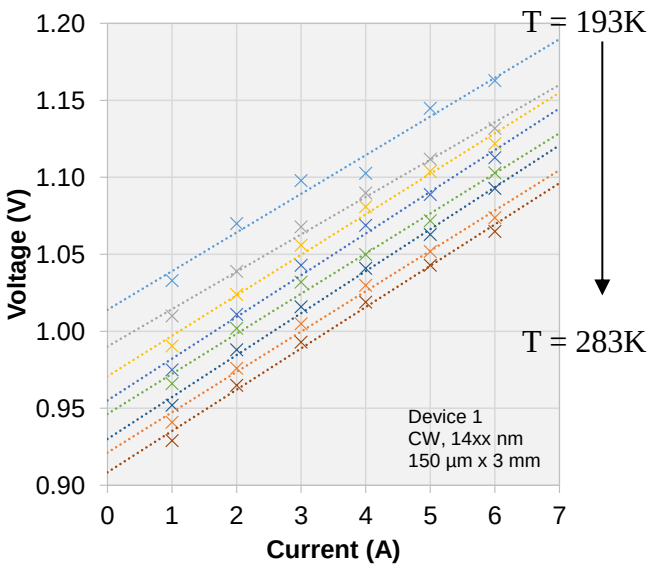

Figure 6.8 **VI curve set for all tested temperatures. Top to bottom: 193K, 223K, 233K, 243K, 253K, 263K, 273K, 283K**

Standard deviation of the voltage measurements as a function of input current is shown below in **Figure 6.9**. The measured voltage as a function of drive current displays a small degree of heteroscedasticity; standard deviation of the diode voltage increases with current.

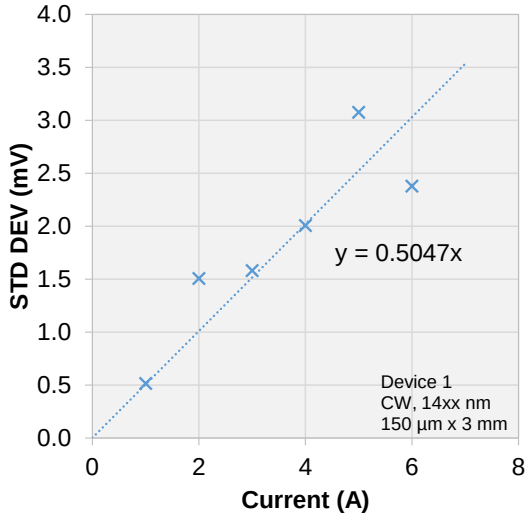

Figure 6.9 **Standard deviation in measured voltage as a function of current.**

To account for the heteroscedasticity of the voltage data, a weighted least squares regression routine is performed. Each data point is weighted by 1/σ (reciprocal of standard deviation, σ) in the manner shown below:

$$\frac{y_i}{\sigma_i} = \frac{x_i}{\sigma_i} + \frac{\epsilon_i}{\sigma_i} \qquad 6.1$$

This weighting scheme for linear regression has the effect of assigning more importance to data with lower standard deviation; data measured at lower currents have larger weights since the associated measurement error is lower and they are more 'trusted'. These two methods of linear regression are performed to extract the zero-voltage (y-intercept of linear fit, turn-on) and series resistance (slope of linear fit) and are shown in **Figure 6.10** below: ordinary least squares (OLS) and weighted least squares as previously described are compared.

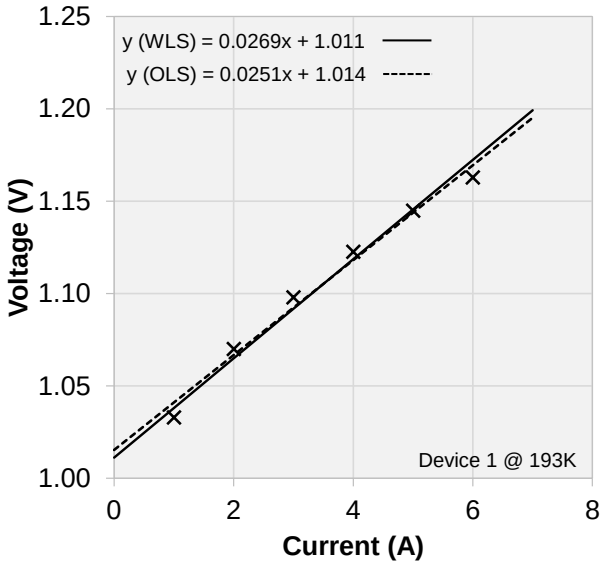

Figure 6.10 Comparison of VI linear fit using ordinary least squares (dotted) and weighted least squares (solid) for 'Device 1: 14xx nm' at 193K

The slope and intercept information extracted from the weighted least squares routine accounts for the heteroscedasticity of the voltage data. The WLS method results in a zero-voltage estimate approximately 2mV smaller than the OLS method: $V_{0,OLS}$ = 1.011mV and $V_{0,WLS}$ = 1.013mV. The series resistance obtained via WLS is .027 ohms. Standard error is propagated through the least squares regressions to associate a prediction uncertainty in the final reported models.

Inspecting the (previously displayed **Figure 6.8**) plots of the voltage-current data for each temperature, a tendency for the measured voltage to depart from linear increase in a similar fashion to the optical power vs. current plots (i.e. measurements stray from the linear trend to lower voltages as a function of current) is apparent. This, too, is a result of self-heating due to thermal resistance: the junction temperature increases at higher input currents, shifting the measured voltages to a higher temperature *VI* curve. A model that accounts for temperature variations due to increased input power (incorporating thermal resistance, R_{th} [K/W], to calculate temperature shift to new voltage line at higher drive currents) would more accurately describe voltage (and light) behavior. For the purpose of extracting V_0 and series resistance information for calculating the *M*-parameter, however, this is not necessary as demonstrated in the following pages.

The effects of temperature on device operation are now apparent: as temperature decreases, threshold current decreases while slope efficiency and diode voltage increase. Series resistance is unchanged with temperature. These qualitative temperature trends are summarized in **Table 6.1** on the following page.

Table 6.1 Operational parameters: qualitative responses to changes in temperature. 'Red' denotes a relative decrease in device efficiency/performance and 'green' denotes an increase.

Parameter	Temperature ↑	Temperature ↓
I_{th}	↑	↓
η	↓	↑
V_0	↓	↑
R_s	-	-

The following figures (**Figure 6.11- Figure 6.13**) show the model approximations to the temperature-dependent operation parameters: $I_{th}(T)$ given by Eq. (4.1) and described by T_0, $\eta(T)$ given by Eq. (4.2) and described by T_1, and V_0, the newly defined linear model described by M.

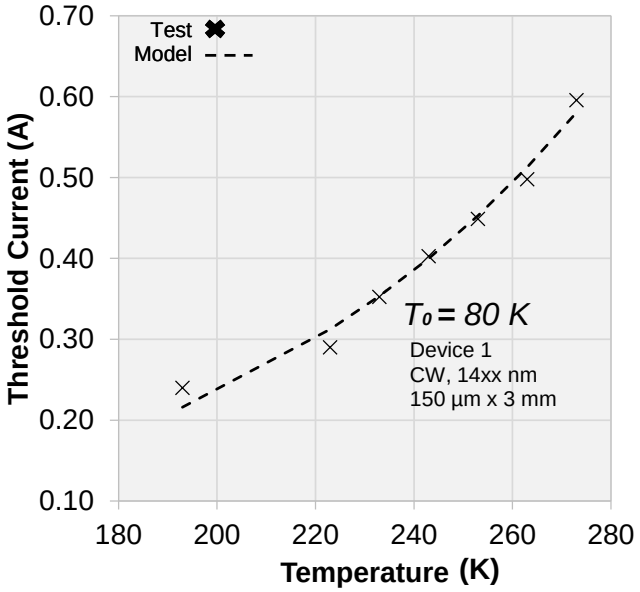

Figure 6.11 Threshold current as a function of temperature is modelled by Eq. (4.1) and temperature parameter T_0

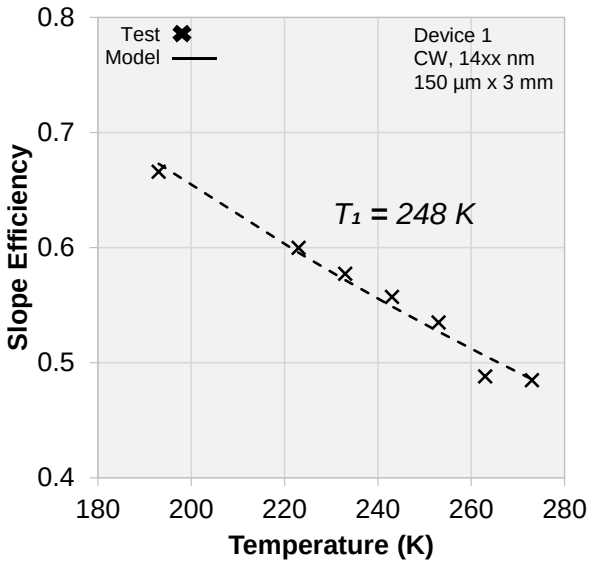

Figure 6.12 Slope efficiency as a function of temperature is modelled by Eq. (4.2) and temperature parameter T_1

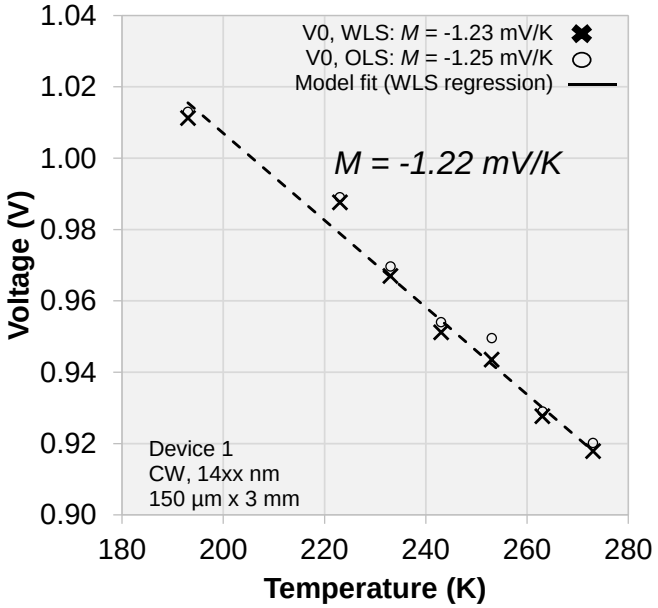

Figure 6.13 'Zero-voltage' is modelled by the newly defined linear $V_0(T)$ aproximation and slope parameter M. V_0 determined from both OLS and WLS routines are shown

The experimentally determined temperature parameters (the model fits in **Figure 6.11 - Figure 6.13**) for sample chip 'Device 1: 14xx nm' are provided in **Table 6.2** below. Using only these parameters, the temperature-dependent LIV curves can be generated. With the parametrically generated LIV data, PCE is calculated and shown to agree well with experimental data.

Table 6.2 Temperature parameters for 'Device 1: 14xx nm' used to generate parametric operation models

Parameter	Value	Units
T_0	80	K
T_1	248	K
M	-1.22	mV/K
R_s	0.027	Ω

Table 6.3 Temperature-dependent data generated using parameters from Table 4 and plotted with experimental data in Figures 6.14 and 6.15.

Temp	Ith	Voltage	SE	Rs
193	0.20	1.0155	0.67	0.027
223	0.30	0.9789	0.60	0.027
233	0.34	0.9667	0.57	0.027
243	0.39	0.9545	0.55	0.027
253	0.45	0.9423	0.53	0.027
263	0.51	0.9301	0.51	0.027
273	0.59	0.9179	0.49	0.027
RMSE	0.015	0.005	0.01	0.001

Light and voltage versus current (LIV) and power conversion efficiency (wallplug efficiency) at any desired temperature within the tested region are fully described with the parameters summarized in **Table 6.3.** The LIV and PCE curves generated for T=193K, 233K, and 273K are compared to experimental data in **Figure 6.14** and **Figure 6.15** below. The approximations show good agreement with experimental data, demonstrating validity of the

established threshold current and slope efficiency parametric models and the newly defined linear voltage model described by the *M*-parameter. LIV and PCE model comparisons for all tested devices are provided in **Appendix A**.

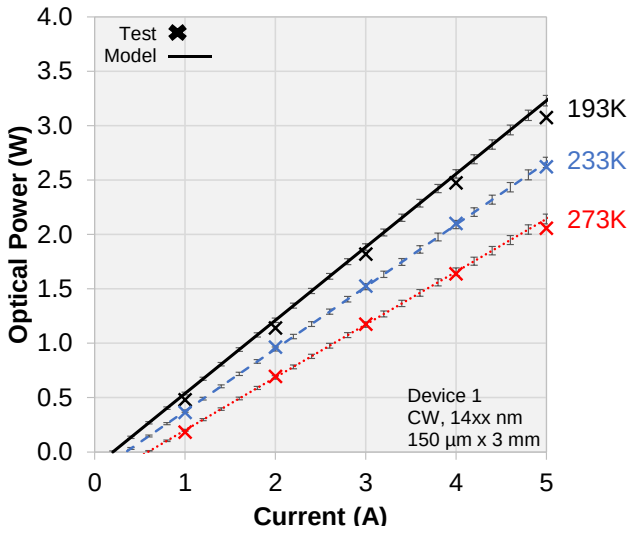

Figure 6.14 **'Device 1: 14xx nm' *LI* experimental data compared to *LI* model generated using temperature parameters. Agrees well for 233K and 273K; model estimation is high for 193K.**

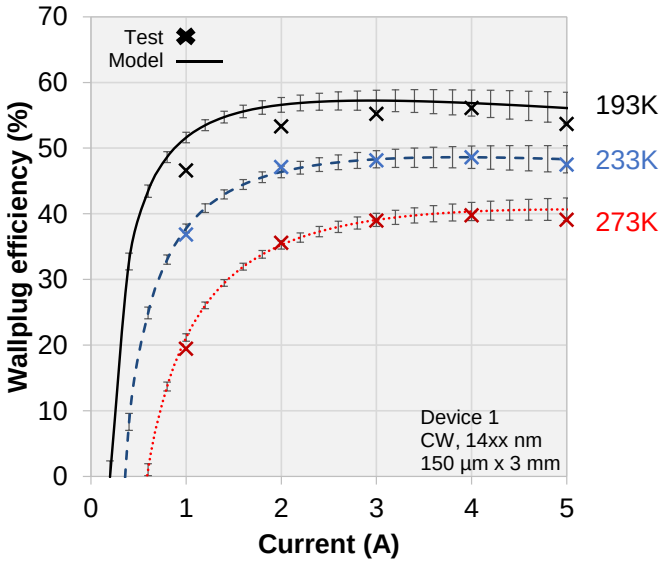

Figure 6.15 **'Device 1: 14xx nm' parametric models (lines) agree well with experimental data at 233K and 273K (x's). Estimated wallplug is higher than experimental at 193K.**

In **Figure 6.15**, the predicted wallplug efficiency at 193K exceeds the measured values by approximately 10%. This is attributed to over-predictions of threshold current and slope efficiency, demonstrated in the LI curves in **Figure 6.14**. These prediction errors in the optical output are due to the T_0 and T_1 model temperature ranges of validity; the exponential models do not appropriately describe threshold current and slope efficiency at lower temperatures.

A sample determination of thermal resistivity for a test device is shown in **Figure 6.16** and **Figure 6.17.** A temperature dependent wavelength shift of 0.5nm/K is assumed to estimate junction temperature using spectral data. Centroid wavelength recorded at each current level enables extraction of temperature increase at each input current. Excess power (difference between input electrical power and output optical power) generates heat which in turn increases junction temperature. Finally, the temperature increase per increase in drive power is calculated, yielding thermal resistance, R_{th} with units of K/W.

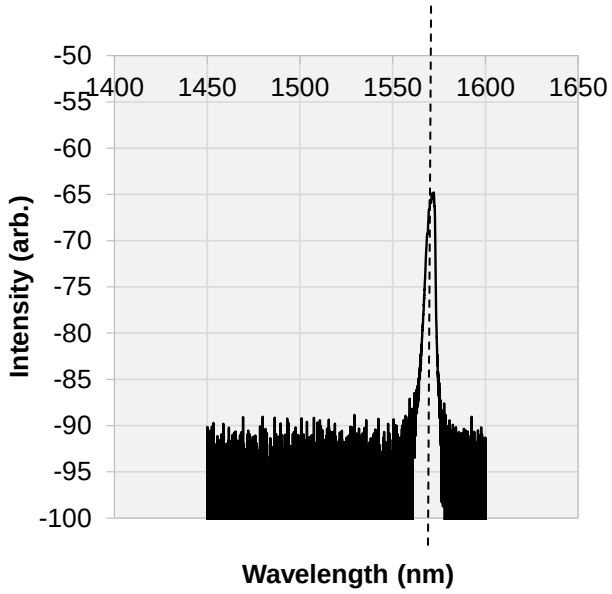

Figure 6.16 Sample spectrum used to determine centroid wavelength at each drive current for a single temperature point

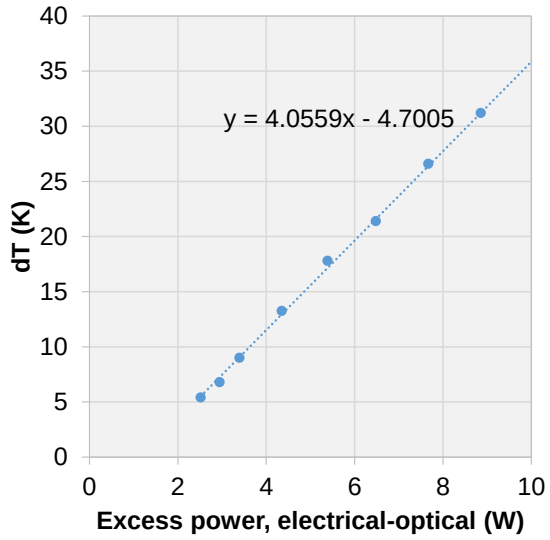

Figure 6.17 Linear fit to change in temperature (found by wavelength shift) vs. excess supply power (difference between electrical and optical power). Slope of this fit is the thermal resistance, R_{th} (K/W)

Several high-power, high-efficiency devices were tested in the cryostat chamber per the method outlined in **Section 5**. Results are summarized in **Table 6.4** below and temperature-dependent operational parameters are reported.

Table 6.4 Summary of temperature terms for characterization of tested devices

Device	T_0 (K)	T_1 (K)	M (mV/K)	R_s (Ω)
DEVICE 1 14xx nm	80	248	-1.22	0.027
DEVICE 2 19xx nm	65	331	-1.14	0.042
DEVICE 3 15xx nm	79	265	-1.04	0.032

7.0 DISCUSSION

7.1 Voltage model validation

The voltage-temperature model, $V_0(T)$ with temperature parameter, M, is shown to agree well with experimental data for the devices characterized at low temperatures. **Figure 7.1** below shows the experimental zero-voltage data with the linear fit with slope M. Over the temperature range tested in the cryostat (193K-283K), the linear trend accurately predicts the diode voltage (+/- 5mV) for 'Device 1: 14xx nm'; the largest error occurs at 223K and equal to 0.43% (1.0054V model prediction vs. 1.0098V experimental).

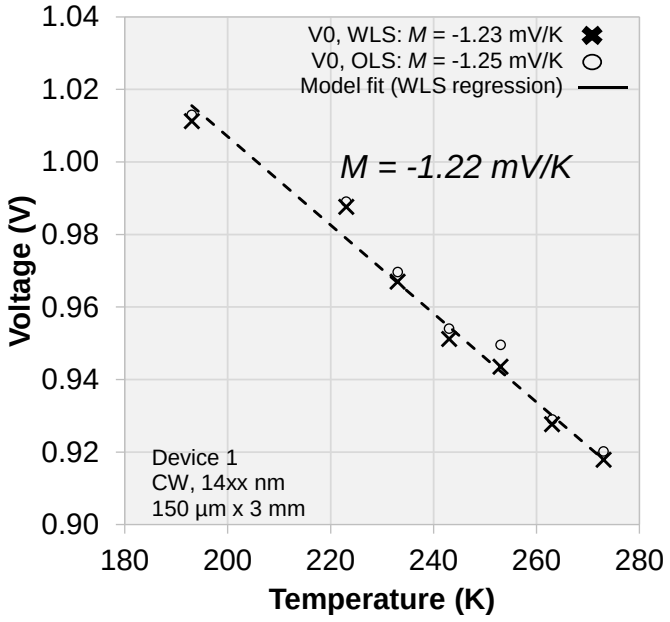

Figure 7.1 'Device 1: 14xx nm' $V_0(T)$ experimental vs. model comparison

The following figure (**Figure 7.2**) demonstrates the agreement of $V(T)$ generated by the V_0 model compared to the experimental data measured at temperatures of 193K, 233K, and 273K.

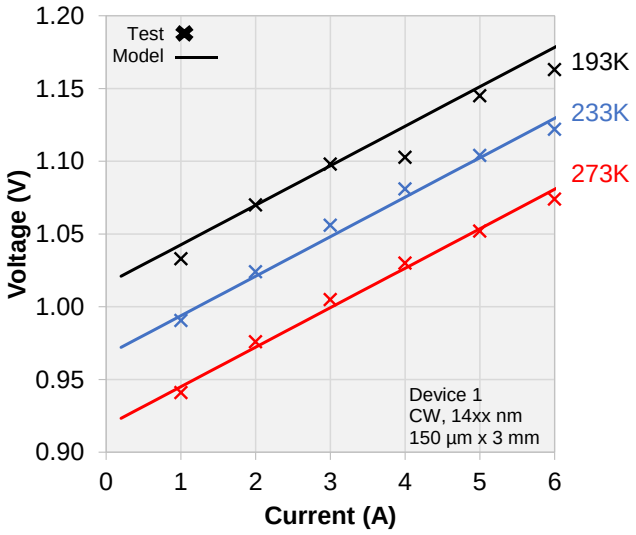

Figure 7.2 Voltage vs. current curves generated using the V_0 model compared to experimental data. Top to bottom: 193K, 233K, 273K.

Next, the established threshold current and slope efficiency models (via T_0 and T_1) are used to generate *LI* data and compared to laboratory results (**Figure 7.3**). Agreement between parametric-model-generated data and experiment is acceptable for temperatures of 233K and 273K. The predicted values for optical power at 193K are consistently high due to over-predicting slope efficiency and under predicting threshold current using the T_0 and T_1 parametric models. This is believed to be caused by assuming model accuracy outside of acceptable temperature regions; slope efficiency cannot increase exponentially as temperature decreases. At low temperatures (e.g. 193K), the exponential models are no longer appropriate for predicting threshold current and slope efficiency.

Finally, power conversion efficiency is calculated and shown in **Figure 7.4** on the following page. Maximum error of 10% over-prediction occurs for the measurements taken at 193K due to model errors in the *LI* data (the previously described violation of temperature range validity for the T_0 and T_1 models). At 233K and 273K, PCE error does not exceed 5%.

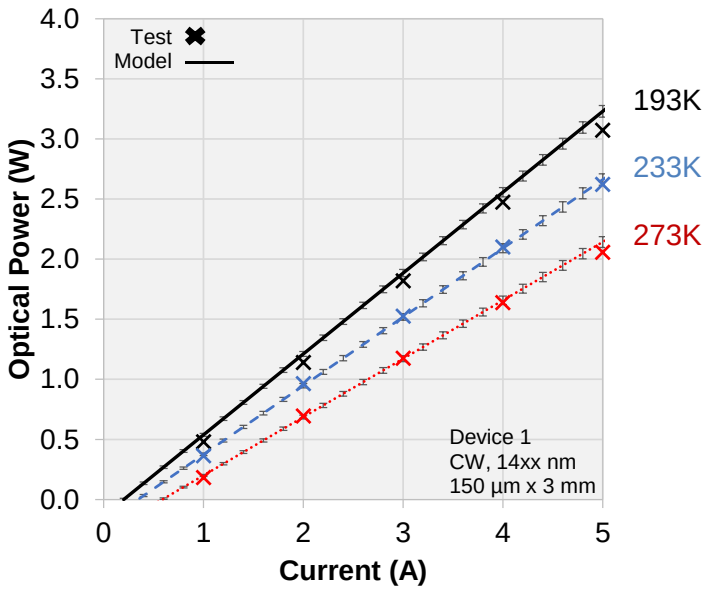

Figure 7.3 **Light-current data generated using threshold current and slope efficiency temperature parameters (lines) compared to laboratory data.**

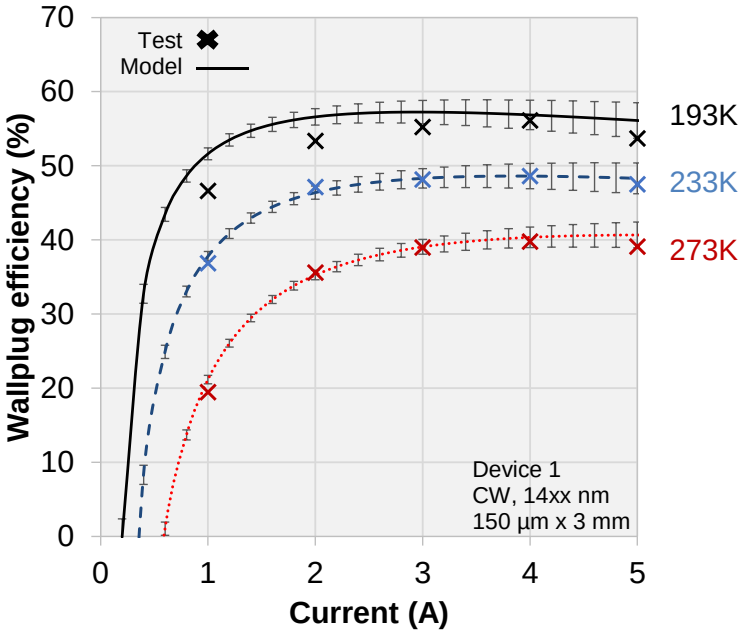

Figure 7.4 **Power conversion efficiency (%) for parametrically generated curves compared to experiment**

The agreement between the PCE data predicted using the temperature parameters for threshold current, slope efficiency, zero-voltage + series resistance and experimental data is acceptable (+/- 3%, sufficient for device benchmarking and characterization predictions); the proposed linear voltage-temperature model is valid. The linear voltage model appropriately predicts voltage over the tested range (down to 193K) and is predicted by the numerical models to be valid to at least 350K (and potentially higher, though only experimentally verified to 300K).

An exploratory analysis of voltage sensitivity to temperature-dependent changes in device parameters at various temperatures was performed using the third order *V(I,T)* model previously described in **Section 4**. First, the percent change in each parameter for an increase in temperature of 1% was found. The change in voltage *V(T)* at a drive current of 3 Amps was then found independently for each parameter's calculated change due to the 1% temperature increase. Voltage sensitivities were normalized to compare each parameter, shown in **Figure 7.5** on the following page. The sensitivities were calculated at three different temperature set points: 193K, 233K and 273K. No significant temperature-dependent changes in parameter sensitivity is present over the inspected temperature range.

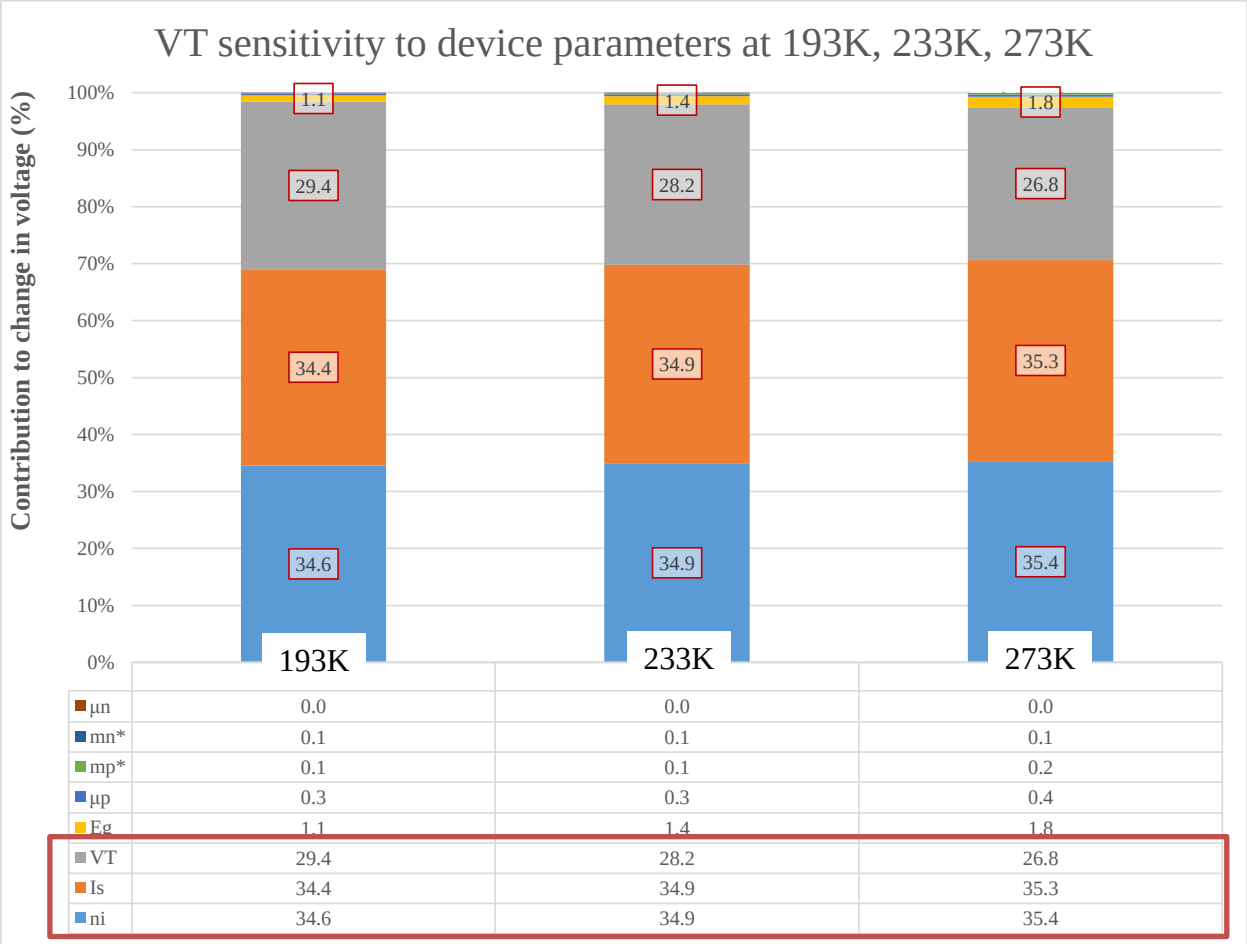

Figure 7.5 Change in voltage due to 1% increase in various parameters are quantified above for operation at 193K, 233K, and 273K

Temperature-dependent voltage changes are most sensitive to intrinsic carrier density, n_i, reverse bias saturation current, I_s, and thermal voltage, V_t (greater than 25% contribution to voltage changes for each parameter). Bandgap, carrier mobility, and carrier effective mass contribute less to changes in voltage as temperature varies (less than 2% total).

8.0 LIMITATIONS AND FUTURE WORK

8.1 Improvements to experiment

The cryostat testing station proved to be a suitable solution for characterizing diode laser performance at low temperatures. However, several aspects of the testing station and data collection process can be improved. Primarily, uncertainty in measured data could be greatly reduced by implementing several modifications to the setup and measurement methods.

A dedicated temperature sensor for in-situ measurement of junction temperature of test devices would enable more accurate temperature readouts. The temperatures reported for the collected data were determined via a temperature sensor mounted to the cold arm of the cryostat. This sensor communicates with the temperature controller to adjust the cryostat heater (balanced by the liquid nitrogen coolant) to reach the desired temperature setpoint. During operation, it is likely that the actual temperature of the diode fixture is higher than the cold-arm sensor displays due to self-heating - especially at high current. A sensor fixed directly to the diode mount would mitigate the uncertainty associated with the reported temperature data.

Optical power loss due to clipping of the fast axis through the cryostat window was calibrated via comparison to the gold-standard room temperature results. For the devices tested in this experiment, this calibration was sufficient. For future tests, however, devices may exhibit a greater fast axis divergence which could result in a greater degree of beam clipping. Additionally, at higher current injection levels higher order modes begin to lase. The lasing of higher order modes further increases the fast axis divergence, resulting in a non-linear change in optical power loss as current increases due to clipping of the beam by the cryostat window. Tests should therefore calibrate power loss as a function of drive current to appropriately account for beam clipping of devices exhibiting especially large fast-axis divergence.

The laboratory test setup consists of numerous components – cryostat, vacuum pumping station, voltage probe DMM, optical thermopile, laser diode power supply, optical spectrum analyzer, and associated miscellaneous mounts and fibers. Manual monitoring and control/placement of each of these devices during data collection often proved to be difficult (and time consuming) and could possibly lead to misread (or not read) data points. Each of the machines involved in the characterization process have the capability for computer control - it would be a worthwhile endeavor to design and implement an automated testing station for future low temperature laboratory work. To this end, Labview would be a suitable control platform.

8.2 **Voltage model considerations**

The newly developed and experimentally validated voltage model is briefly discussed in **Sections 6** and **7**. A linear approximation is shown to be sufficient to describe temperature-dependent voltage behavior of laser diodes. A more thorough investigation of the linear model and the underlying physics that corroborate the linear trend, is a great starting point for future low temperature diode design work. Teasing out the intricacies of a full 3rd order temperature model with a comparison to the simple linear model would offer insight into the critical parameters governing device performance. Developing a better understanding of these mechanisms and their response to design changes is a promising research endeavor for implementing new diode laser designs for ultra-high performance devices.

9.0 CONCLUSION

Three eye-safe diode laser devices were characterized at low temperatures using a liquid nitrogen cooled cryostat setup. Established empirical models used to predict threshold current and slope efficiency as a function of temperature were validated using the low temperature experimental data. For especially low temperature tests, the empirical models for optical power characteristics (T_0 and T_1) are shown to over-predict threshold current and slope efficiency. This results in an over-prediction of wallplug efficiency at low temperatures. A new empirical model and temperature parameter, $V_0(T)$ modelled with the now defined *M*-parameter, was developed and shown to adequately describe tested device voltage behavior. This voltage-temperature model enables an accurate, simple description of device performance over a wide range of test temperatures (193K – 300K in the tested data, greater than 350K numerically modelled). A full analysis of the complex temperature-dependent voltage physics governing semiconductor laser devices for performance prediction is avoided by defining the *M*-parameter for a given laser diode.

The *M*-parameter coupled with T_0 and T_1 enables prediction of power conversion efficiency as a function of temperature, a critical laser performance metric. Predictions of wallplug efficiency compared to experimental data are shown to be accurate down to 233K. At lower temperatures (193K experimentally), the optical characteristic parameters (T_0 and T_1 using exponential models for threshold current and slope efficiency) are no longer valid, though the *M*-parameter still adequately describes diode voltage. Future work aimed to analyze and develop ultra-high efficiency diode lasers will benefit from the implementation of the $V_0(T)$ device description and characteristic *M*-parameter.

LIST OF REFERENCES

[1] "Laser Diode Modules." Newport. ILX Lightwave, n.d. Web. 10 Aug. 2016.

[2] Gale, Patrick. "Estimating Laser Diode Lifetimes and Activation Energy." ILX Lightwave Application Note AN33. 2008

[3] Paschotta, Rüdiger. "Laser Diodes." Encyclopedia of Laser Physics and Technology. RP Photonics, Web. 10 Aug. 2016

[4] "Diode Lasers." *Coherent Inc. Laser Diode, High Power Laser Diodes, Diode Laser*. Coherent Inc., Web. 30 Aug. 2016.

[5] Steele, Robert V. "Diode-laser market grows at a slower rate". Laser Focus World. 41. 2005

[6] Kincade, Kathy; Stephen Anderson (2005). "Laser Marketplace 2005: Consumer applications boost laser sales 10%". Laser Focus World. 41 (1). Archived from the original on June 28, 2006

[7] Dawson, Jay W. and Crane, John K. and Messerly, Michael J. and Prantil, Matthew A. and Pax, Paul H. and Sridharan, Arun K. and Allen, Graham S. and Drachenberg, Derrek R. and Phan, Henry H. and Heebner, John E. and Ebbers, Christopher A. and Beach, Raymond J. and Hartouni, Edward P. and Siders, Craig W. and Spinka, Thomas M. and Barty, C. P. J. and Bayramian, Andrew J. and Haefner, Leon C. and Albert, Felicie and Lowdermilk, W. Howard and Rubenchik, Alexander M. and Bonanno, Regina E., *High average power lasers for future particle accelerators*. AIP Conference Proceedings, 1507, 147-153. 2012

[8] Coldren, Larry A., Scott W. Corzine, and Milan L. Mashanovitch. *Diode Lasers and Photonic Integrated Circuits, 2nd Edition*: John Wiley & Sons, 2012

[9] Zhigang Chen ; Weimin Dong ; Xingguo Guan ; Sandrio Elim ; Shiguo Zhang ; Mike Grimshaw ; Mark Devito ; Paul Leisher ; Manoj Kanskar; *76% efficient cryogenically- cooled eyesafe diode laser for resonant pumping of Er-doped gain media*. Proc. SPIE 8640, Novel In-Plane Semiconductor Lasers XII, 86401L. March 4, 2013

[10] Paul Crump, Mike Grimshaw, Jun Wang, Weimin Dong, Shiguo Zhang, Suhit Das, Jason Farmer, Mark Devito, Lei Meng, and Jason Brasseur. *85% Power Conversion Efficiency 975-nm Broad Area Diode Lasers at – 50°C, 76 % at 10°C.* Optical Society of America. 2006

[11] Fonstad, C. G. "Lecture 20 - Laser Diodes 1." MIT OC. MIT, Web. April, 2003

[12] Van Zeghbroeck, Bart J. *Principles of Semiconductor Devices*. 2.5 Carrier Density and the Fermi Energy. ECEE CU Boulder. Web. 10 Aug. 2016

[13] "Diode Laser Heatsinks". *AliExpress*. n.d. Web. 30 August, 2016

[14] "6000 Series Portable Chillers" *Chillers and Coolers*. Polyscience, n.d. Web. 30 Aug. 2016.

[15] Toshio Higashi, Stephen J. Sweeney, Alistair F. Phillips, Alfred R. Adams, Eoin P. O'Reilly, Toru Uchida, and Takuya Fujii, *Experimental Analysis of Temperature Dependence in 1.3- m AlGaInAs–InP Strained MQW Lasers*. IEEE J. Sel Topics Quant Electron 5, 413-419. 1999

[16] P. Abraham, J. Piprek, S. P. DenBaars, and J. E. Bowers. *Study of Temperature Effects on Loss Mechanisms in 1.55 μm Laser Diodes with InGaP Electron Stopper Layer*. Semiconductor Science and Technology vol. 14, no. 5, pp. 419-424. January 1, 1999

[17] O'Reilly, E. P., Jones, G., Silver, M. and Adams, A. R. *Determination of Gain and Loss Mechanisms in Semiconductor Lasers Using Pressure Techniques*. Phys. Status Solidi B, 198: 363–373. 1996

[18] Y. Zou et al., *Experimental study of Auger recombination, gain, and temperature sensitivity of 1.5 μm compressively strained semiconductor lasers.* IEEE Journal of Quantum Electronics, vol. 29, no. 6, pp. 1565-1575, June 1993

[19] Paul Crump, Jun Wang, Trevor Crum, Suhit Das, Mark DeVito, Weimin Dong, Jason Farmer, Yan Feng, Mike Grimshaw, Damian Wise, Shiguo Zhang *> 360W and > 70% Efficient GaAs-Based Diode Lasers*. Proceedings of Photonics West, High-Power Diode Laser Technology and Applications III, Proc SPIE 5711. 2005

[20] E. Yablonovitch and E. O. Kane. *Band structure engineering of semiconductor lasers for optical communications.* Journal of Lightwave Technology, vol. 6, no. 8, pp. 1292-1299, Aug 1988

[21] C. Henry, R. Logan, F. Merritt and J. Luongo. *The effect of intervalence band absorption on the thermal behavior of InGaAsP lasers*. IEEE Journal of Quantum Electronics, vol. 19, no. 6, pp. 947-952, June 1983

[22] P. O. Leisher, W. Dong, M. P. Grimshaw, M. J. DeFranza, M. A. Dubinskii and S. G. Patterson. *Mitigation of Voltage Defect for High-Efficiency InP Diode Lasers Operating at Cryogenic Temperatures*. IEEE Photonics Technology Letters, vol. 22, no. 24, pp. 1829-1831, Dec. 2010

[23] Bai Y, Bandyopadhyay N, Tsao S, Selcuk E, Slivken S, Razeghi M. *Highly temperature insensitive quantum cascade lasers*. Appl. Phys. Lett. 97(25). 2010

[24] Barber, H.D. *Effective Mass and Intrinsic Concentration in Silicon.* Solid State Electronics, v. 10, no. 11, p 1039-1051. Nov. 1967

[25] Pierret, Robert F. *Semiconductor Device Fundamentals*. Reading, MA: Addison-Wesley, 1996

APPENDICES

APPENDIX A: PARAMETER FITS, LIV/PCE COMPARISONS FOR TESTED DEVICES

APPENDIX B: MANUFACTURER SPECIFICATION OF CRYOSTAT WINDOW REFLECTANCE

APPENDIX C: MATLAB CODE USED FOR TEMPERATURE-DEPENDENT PARAMETRIC MODELS

APPENDIX A: PARAMETER FITS, LIV/PCE COMPARISONS FOR TESTED DEVICES

DEVICE 1: 14XX NM

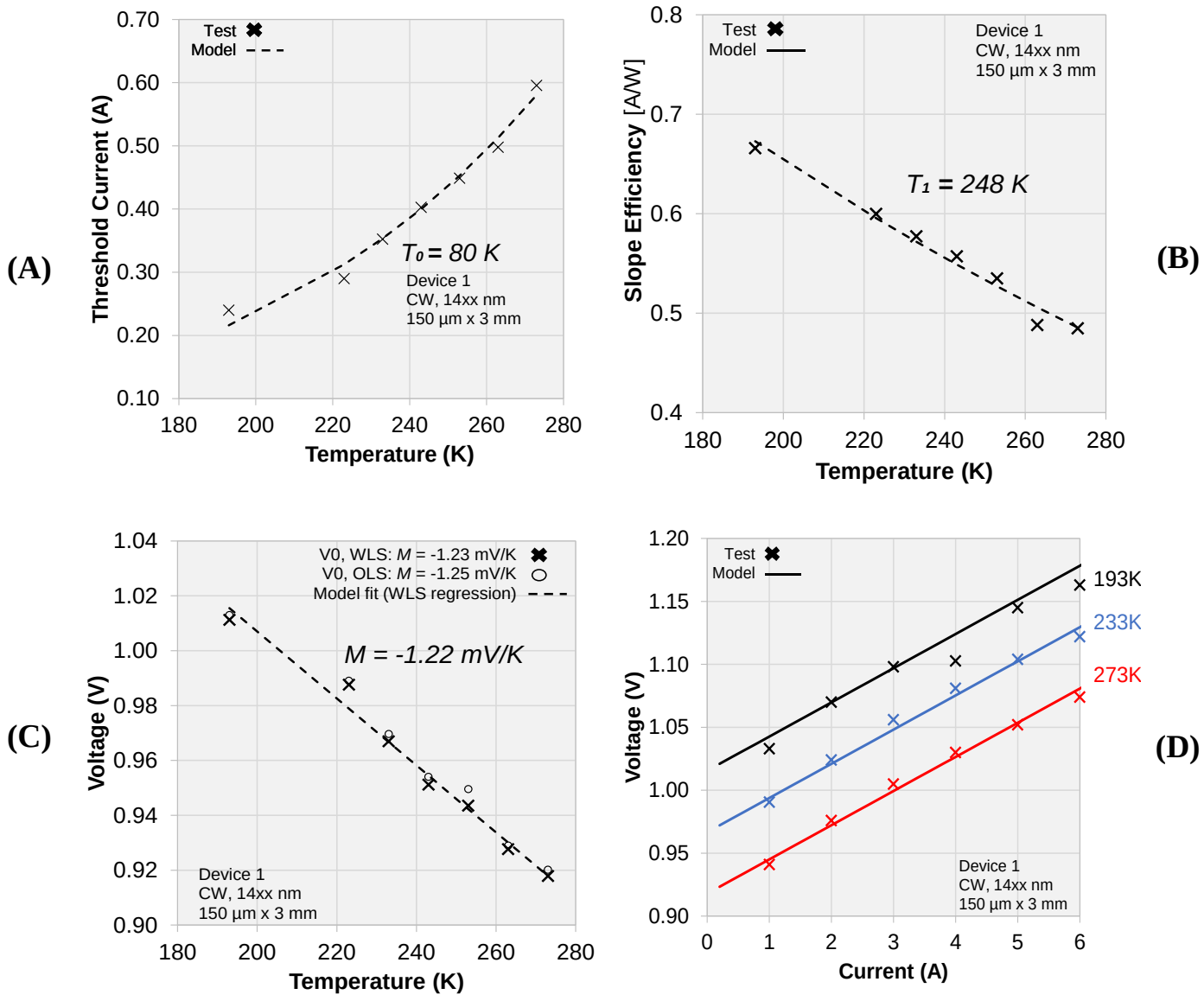

Figure A.1 'Device 1: 14xx nm': (A) Threshold current data and T_0 model comparison. (B) Slope efficiency data and T_1 model comparison. (C) Zero voltage data and *M*-parameter model comparison. (D) *VI* curve comparison of experimental data and linear model + series resistance fit

DEVICE 1: 14XX NM

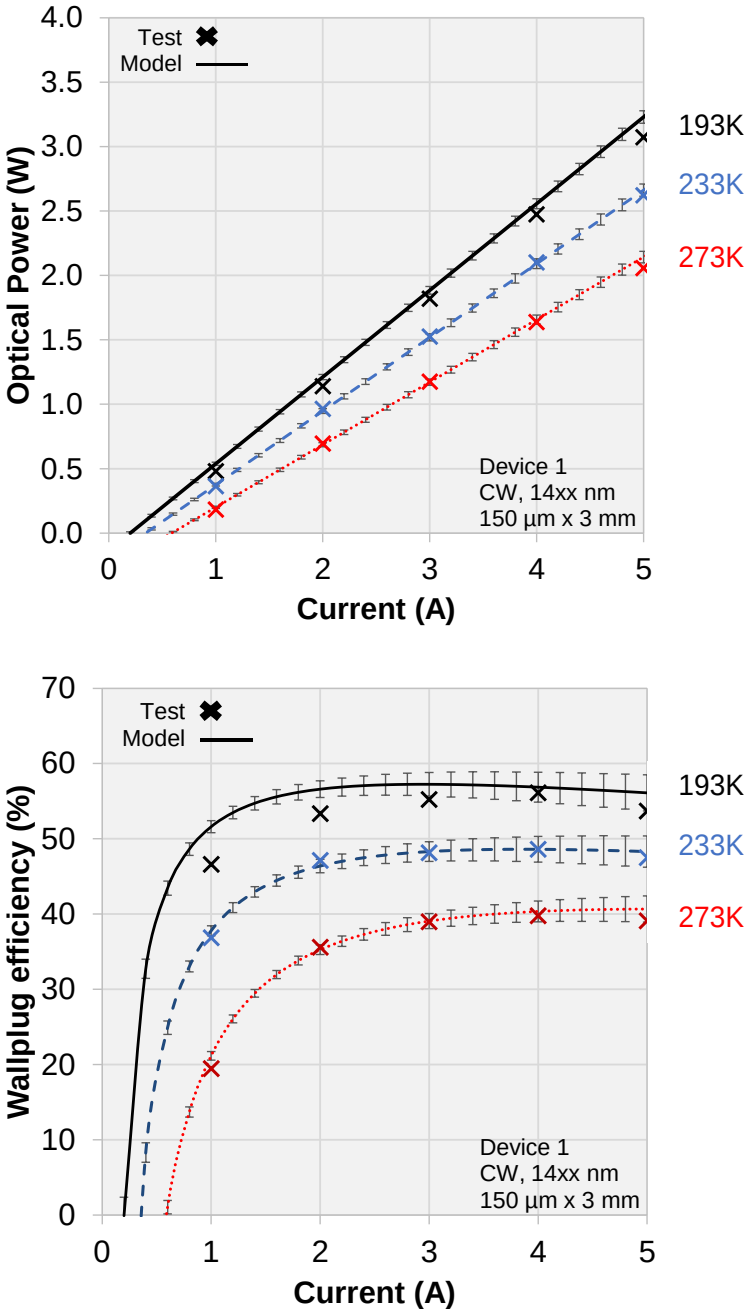

Figure A.2 **'Device 1: 14xx nm': Top: *LI* curve comparing experimental data and predicted values using empircal models. Bottom: Comparison of experimental power conversion efficiency to predicted PCE (using empircal models)**

DEVICE 2: 19XX NM

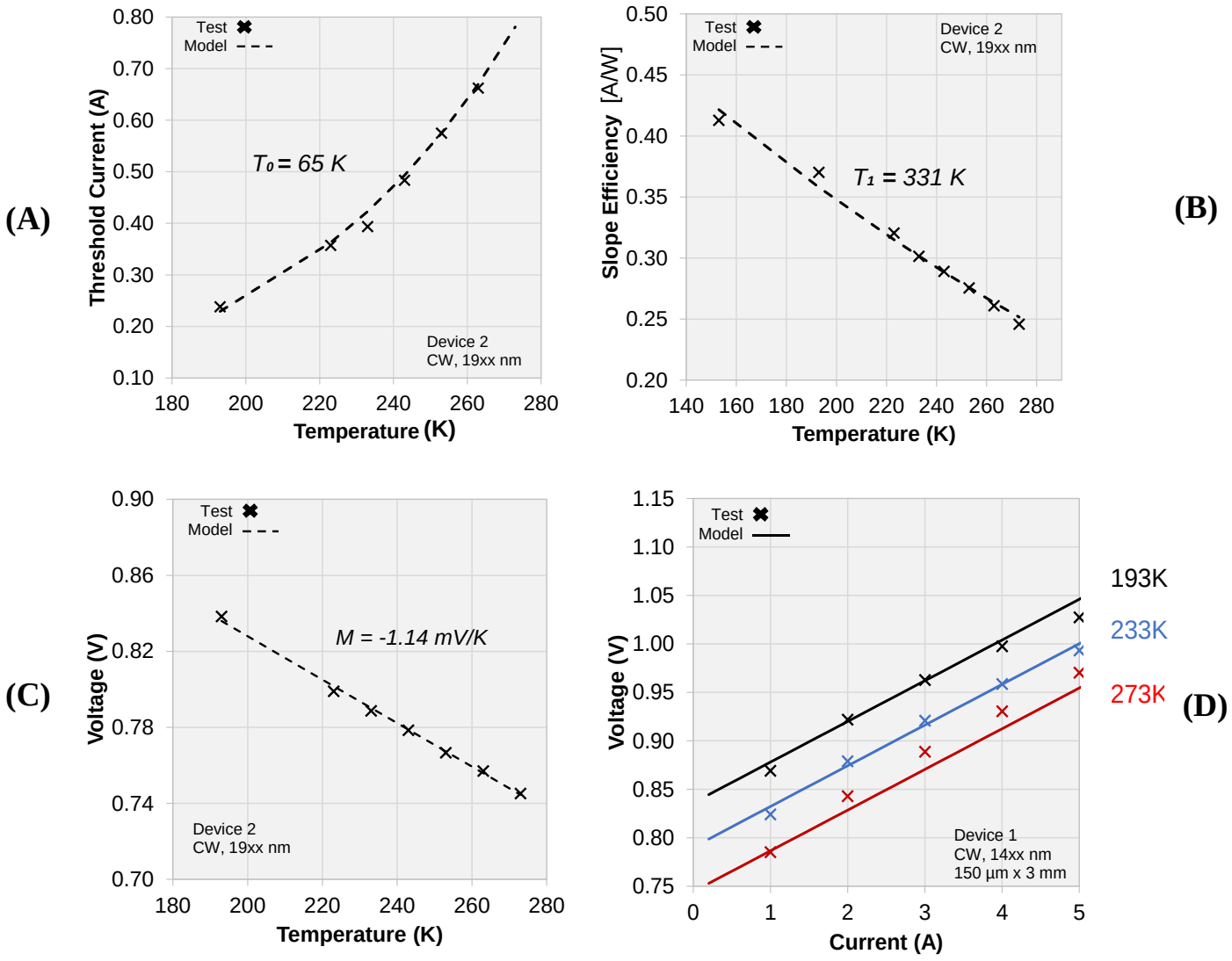

Figure A.3 **'Device 2: 19xx nm': (A) Threshold current data and T_0 model comparison. (B) Slope efficiency data and T_1 model comparison. (C) Zero voltage data and *M*-parameter model comparison. (D) *VI* curve comparison of experimental data and linear model + series resistance fit**

DEVICE 2: 19XX NM

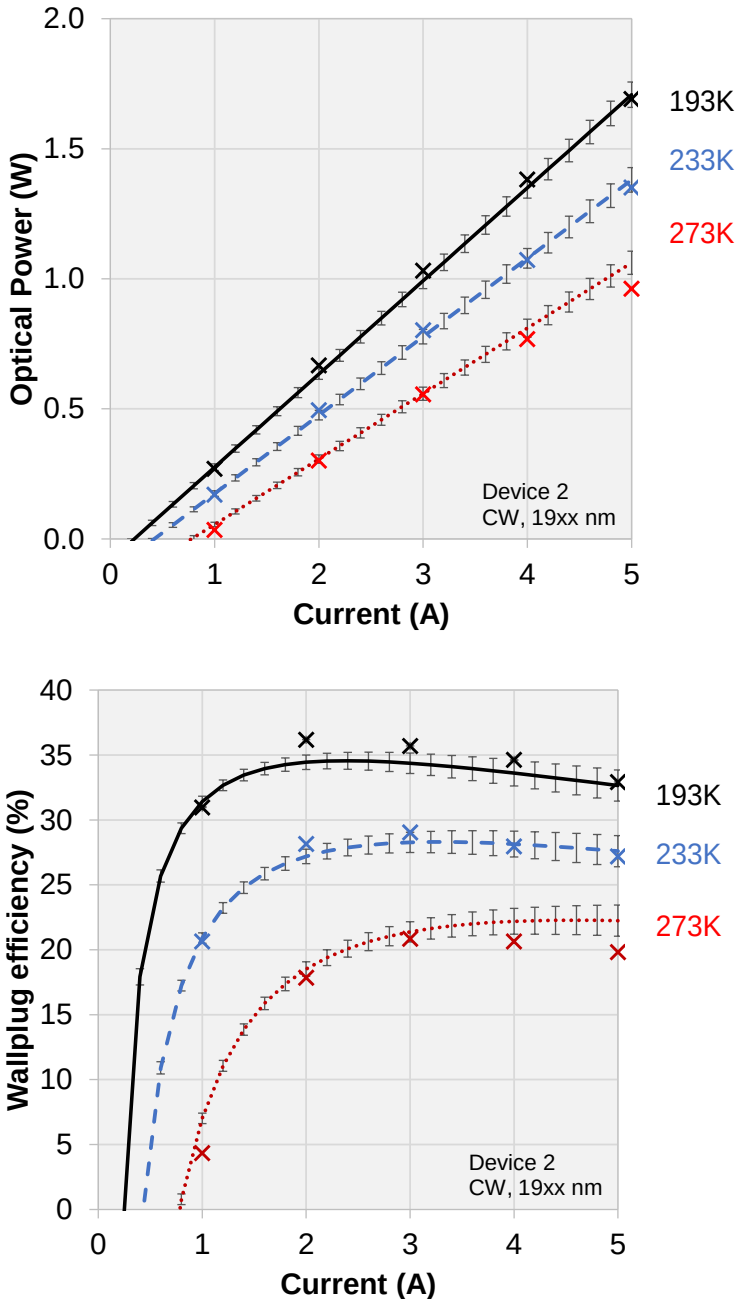

Figure A.4 **'Device 2: 19xx nm': Top: *LI* curve comparing experimental data and predicted values using empircal models. Bottom: Comparison of experimental power conversion efficiency to predicted PCE (using empircal models)**

DEVICE 3: 15XX NM

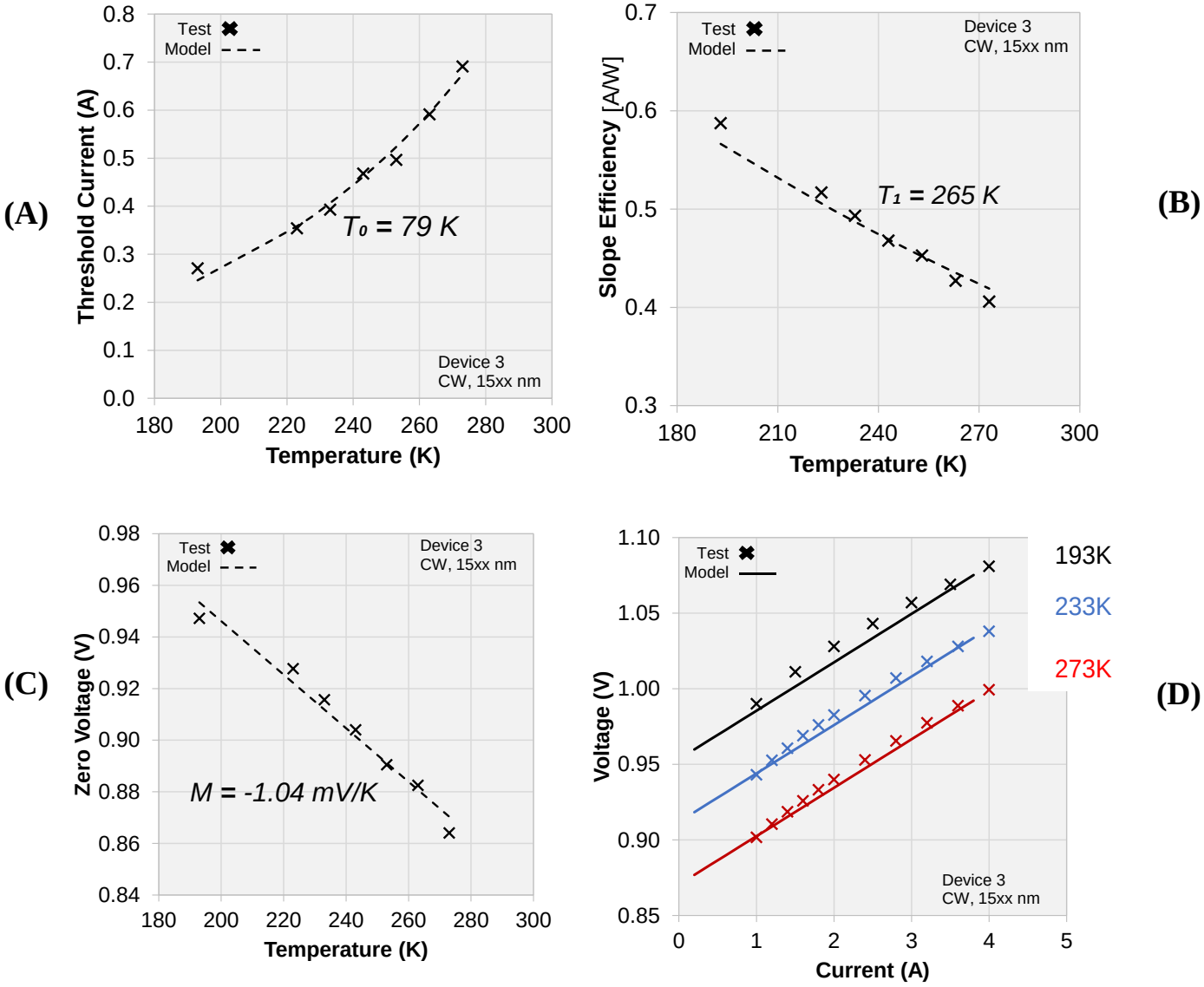

Figure A.5 **'Device 3: 15xx nm': (A) Threshold current data and T_0 model comparison. (B) Slope efficiency data and T_1 model comparison. (C) Zero voltage data and *M*-parameter model comparison. (D) *VI* curve comparison of experimental data and linear model + series resistance fit**

DEVICE 3: 15XX NM

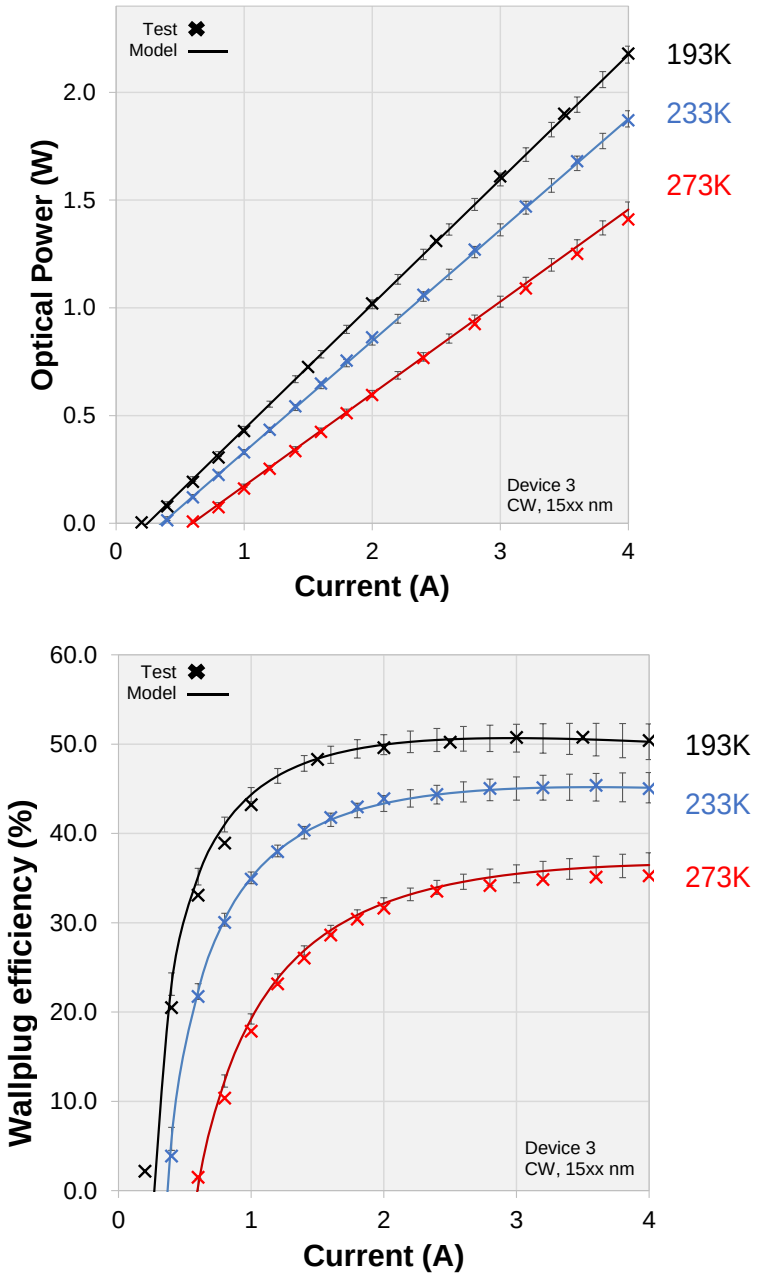

Figure A.6 **'Device 3: 15xx nm': Top: *LI* curve comparing experimental data and predicted values using empircal models. Bottom: Comparison of experimental power conversion efficiency to predicted PCE (using empircal models)**

APPENDIX B: MANUFACTURER DATA FOR CRYOSTAT REFLECTANCE

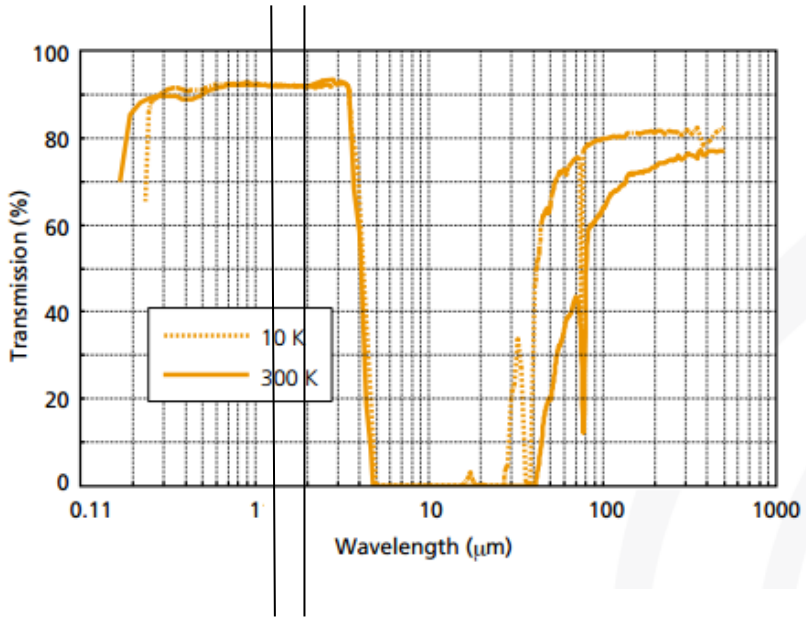

Figure B.1 **Over the range of tested wavelengths, (eye-safe region 1.5-2.0 um in bars above), the reflectance of the cryostat window varies by less than 1% for every tested temperature**

APPENDIX C: MATLAB CODE DEVELOPED FOR TEMPURATURE-DEPENDENT ANALYSIS OF CURRENT AND VOLTAGE CHARACTERISTICS OF LASER DIODES

```
% PN_Voltage_v_current_for_temperature.m
% by Grant Brodnik
%
% finds the voltage across a forward biased PN junction diode for a given
% input current (provide I vector), at various temperatures
% First order, second order, and higher order evaluations possible


%
%

tic
% clc
close all

file = 'C:\Users\brodnigm\Documents\Courses\Thesis\Lab Data\D1 14xx and D2
19xx power, efficiency curves with voltage, window corrections.xlsx';
I0 = 0;
dI = .01;
I_f = 6;
I = I0:dI:I_f;

temp_vec = [100:20:300];
T0 = 300;
Rs_0 = .01;
Eg0 = 2;

dRs_dI = 0.01;
Rs_14xx = .018;
Rs_19xx = .03;
Eg0_14xx = 1.4;
Eg0_19xx = 1.8;

len_T = length(temp_vec);
len_I = length(I);

% Initialize vectors for voltage v current, intrinsic&Is v temperature
V1_T = zeros(len_T,len_I);
V2_T = zeros(len_T,len_I);
V3_T = zeros(len_T,len_I);

V2_T_D1 = zeros(len_T,len_I);
V3_T_D1 = zeros(len_T,len_I);
V2_T_D2 = zeros(len_T,len_I);
V3_T_D2 = zeros(len_T,len_I);
```

```
ni_1O = zeros(len_T,1);
ni_2O = zeros(len_T,1);
ni_3O = zeros(len_T,1);

Is_1O = zeros(len_T,1);
Is_2O = zeros(len_T,1);
Is_3O = zeros(len_T,1);


% color map for lines display
color = jet(len_T);

% create figure windows for plots
hold on
figure(1)

    for i = 1:1:len_T
        [V2_T(i,:),ni_2O(i,1),Is_2O(i,1)] =
second_order(I,Rs_0,temp_vec(i),T0,Eg0);
        [V3_T(i,:),ni_3O(i,1),Is_3O(i,1)] =
third_order(I,Rs_0,temp_vec(i),Eg0);
        [V3_T_D1(i,:),ni_3O(i,1),Is_3O(i,1)] =
third_order(I,Rs_14xx,temp_vec(i),Eg0_14xx);
        [V2_T_D1(i,:),ni_2O(i,1),Is_2O(i,1)] =
second_order(I,Rs_14xx,temp_vec(i),T0,Eg0_14xx);
        [V3_T_D2(i,:),ni_3O(i,1),Is_3O(i,1)] =
third_order(I,Rs_19xx,temp_vec(i),Eg0_19xx);

        [V2_T_D2(i,:),ni_2O(i,1),Is_2O(i,1)] =
second_order(I,Rs_19xx,temp_vec(i),T0,Eg0_19xx);
        [V1_T(i,:),ni_1O(i,1),Is_1O(i,1)] =
first_order(I,Rs_0,temp_vec(i),T0,Eg0);
%
        figure(1)
        plot(I,abs(V1_T(i,:)),'Color',color(i,:))
        plot(I,abs(V2_T(i,:)),'Color',color(i,:))
        plot(I,abs(V3_T(i,:)),'Color',color(i,:))
        xlabel('Current [A]')
        ylabel('Voltage [V]')
        axis([0 6 0 2])
    end

Mv = (V3_T_D1(11,3/dI)-V3_T_D1(6,3/dI))/(temp_vec(11)-temp_vec(6))
V3_T_D1(1,3/dI)

figure(2)
semilogy(temp_vec,ni_1O(:,1),temp_vec,ni_2O(:,1),'b',temp_vec,ni_3O(:,1),'k--
')
% title('Intrinsic v temp,')
xlabel('Temperature [K]')
ylabel('Intrinsic carrier density, n_i [cm^-3]')
axis([160 320 1e2 1e12])
grid
```

```
figure(3)
semilogy(temp_vec,Is_1O(:,1),temp_vec,Is_2O(:,1),'b',temp_vec,Is_3O(:,1),'k--
')
% title('Reverse bias saturation current v temp')
xlabel('Temperature')
ylabel('Reverse bias saturation current [A]')
axis([160 320 1e-35 1e-10])
grid

% ------------------------------------------------------------------------ %
% Data comparison

I_tested = 1:1:12;
frmt_spc = '%f';

file_list = {'D1_V_T_temp_vec.txt';'D2_V_T_temp_vec.txt';...
    'D1_193_L.txt';'D1_233_L.txt';'D1_273_L.txt';...
    'D1_V_T_1.txt';'D1_V_T_3.txt';'D1_L_T_3.txt';'D1_L_T_6.txt';...
    'D1_193_V.txt';'D1_233_V.txt';'D1_273_V.txt';...

    'D2_V_T_1.txt';'D2_V_T_3.txt';'D2_L_T_3.txt';'D2_L_T_6.txt';...
    'D2_193_V.txt';'D2_233_V.txt';'D2_273_V.txt';...
    'D2_193_L.txt';'D2_233_L.txt';'D2_273_L.txt'};

vec_names = {'D1_V_T_temp_vec';'D2_V_T_temp_vec';...
    'D1_193_L';'D1_233_L';'D1_273_L';...
    'D1_V_T_1';'D1_V_T_3';'D1_L_T_3';'D1_L_T_6';...
    'D1_193_V';'D1_233_V';'D1_273_V';...

    'D2_V_T_1';'D2_V_T_3';'D2_L_T_3';'D2_L_T_6';...
    'D2_193_V';'D2_233_V';'D2_273_V';...
    'D2_193_L';'D2_233_L';'D2_273_L'};

num_files = length(file_list);

for i = 1:1:num_files
    file_ID = fopen(char(file_list(i)),'r');
    assignin('base',char(vec_names(i)),fscanf(file_ID,frmt_spc))
    fclose(file_ID);
end

%------------------------------------------------------------------------ %
%Voltage vs. temperature for various current
figure(4)
plot(temp_vec,V2_T_D1(:,3/dI),'r',temp_vec,V2_T_D1(:,1/dI),'b',...
    temp_vec,V3_T_D1(:,3/dI),'r--',D1_V_T_temp_vec,D1_V_T_3,'x red',...
    temp_vec,V3_T_D1(:,1/dI),'b--',D1_V_T_temp_vec,D1_V_T_1,'x blue')
axis([150 300 .75 1.5])
title('D1 14xx voltage vs temp for I = 1A, 3A')
xlabel('Temperature [K]')
ylabel('Voltage [V]')
```

```
figure(5)
plot(temp_vec,V2_T_D2(:,3/dI),'b',temp_vec,V2_T_D2(:,1/dI),'r',...
    temp_vec,V3_T_D2(:,3/dI)','b--',...%D2_V_T_temp_vec,D2_V_T_3,'x blue',...
    temp_vec,V3_T_D2(:,1/dI)','r--')%,D2_V_T_temp_vec,D2_V_T_1,'x red')
axis([100 350 .75 1.25])
title('D2 19xx voltage vs temp for I = 1A, 3A')
% ------------------------------------------------------------------------ %


% ------------------------------------------------------------------------ %
% Light vs. temperature for various current
figure(6)
plot(D1_V_T_temp_vec,D1_L_T_3,'blue',D1_V_T_temp_vec,D1_L_T_6,'red')
axis([150 350 0 4])
title('D1 14xx light vs temp for I = 3A, 6A')

figure(7)
plot(D2_V_T_temp_vec,D2_L_T_3,'blue',D2_V_T_temp_vec,D2_L_T_6,'red')
axis([100 350 0 2.5])
title('D2 19xx light vs temp for I = 3A, 6A')
% ------------------------------------------------------------------------ %


% ------------------------------------------------------------------------ %
% Voltage vs current for both devices
figure(8)
plot(I_tested,D1_193_V,'x blue',...
    I_tested,D1_233_V,'x green',...
    I_tested,D1_273_V,'x red',...
    I,third_order(I,Rs_14xx,193,Eg0_14xx),'b',...
    I,third_order(I,Rs_14xx,233,Eg0_14xx),'g',...
    I,third_order(I,Rs_14xx,273,Eg0_14xx),'r')
axis([0 12 0.8 1.4])
title('D1 14xx Voltage vs current for T = 193, 233, 273')
xlabel('Current (A)')
ylabel('Voltage (V)')

figure(9)
plot(I_tested(1:10),D2_193_V,'x blue',...
    I_tested(1:10),D2_233_V,'x green',...
    I_tested(1:10),D2_273_V,'x red',...
    I,third_order(I,Rs_19xx,193,Eg0_19xx),'b',...
    I,third_order(I,Rs_19xx,233,Eg0_19xx),'g',...
    I,third_order(I,Rs_19xx,273,Eg0_19xx),'r')
axis([0 12 0.6 1.4])
title('D2 19xx Voltage vs current for T = 193, 233, 273')
% ------------------------------------------------------------------------ %


% ------------------------------------------------------------------------ %
% Light vs current for both devices
figure(10)
plot(I_tested,D1_193_L,'x blue',...
    I_tested,D1_233_L,'x green',...
```

```
    I_tested,D1_273_L,'x red')
title('D1 14xx Light vs current for T = 193, 233, 273')
axis([0 12 0 7])
grid

figure(11)
plot(I_tested(1:10),D2_193_L,'x blue',...
    I_tested(1:10),D2_233_L,'x green',...
    I_tested(1:10),D2_273_L,'x red')
title('D1 19xx Light vs current for T = 193, 233, 273')
axis([0 10 0 4])
grid
% ------------------------------------------------------------------------ %


% ------------------------------------------------------------------------ %
% Efficiency vs current for both devices
D1_193_eff = 100.*(D1_193_L./(D1_193_V.*I_tested'));
D1_193_eff_max = zeros(1,length(I_tested));
D1_193_eff_max(1,:) = max(D1_193_eff);

figure(12)
plot(I_tested,D1_193_eff,'x blue',...%I_tested,D1_193_eff_max,'b--',...
    I_tested,100.*(D1_233_L./(D1_233_V.*I_tested')),'x green',...
    I_tested,100.*(D1_273_L./(D1_273_V.*I_tested')),'x red')
title('D1 14xx Efficiency vs current for T = 193, 233, 273')
axis([0 12 0 100])
grid

figure(13)
plot(I_tested(1:10),100.*(D2_193_L./(D2_193_V.*I_tested(1:10)')),'x blue',...
    I_tested(1:10),100.*(D2_233_L./(D2_233_V.*I_tested(1:10)')),'x green',...
    I_tested(1:10),100.*(D2_273_L./(D2_273_V.*I_tested(1:10)')),'x red')
title('D2 19xx Efficiency vs current for T = 193, 233, 273')
axis([0 12 0 100])
grid
% ------------------------------------------------------------------------ %

num_fig = 13;

    for i = 1:1:num_fig
        figure(i)
        position_figure(3,4,i)
    end

toc
```

```
% third_order accepts several physical constants and third order
% device parameters, as well as a vector of drive current and vecotr of
% second order reverse bias saturation current


function [VT,ni,Is_3O] = third_order(current_vector,Rs,T,Eg0)

q = 1.602e-19;
k = 1.38e-23;
Vt = (k*T)/q;
disp(Vt)
% Vt = Vt*1.01;
I = current_vector;

Nd = 1e18; %doping
% Nd = Nd*1.01;
Na = 1e18; %doping
% Na = Na*1.01;

A = 2.510e19; %what is this?
Eex = 0.0074;
% Eg0 = 1.2;
cavity_length = 0.3; %cm
cavity_width = 1e-2; %cm

%Bandgap vs T
a = 4.73e-4;
b = 636;
Eg = Eg0-a*300^2/(300+b);
% Eg = Eg*1.01;

%Effective mass vs T
mnr = 1.028+(6.11e-4)*T-(3.09e-7)*T^2;
mpr = 0.610+(7.83e-4)*T-(4.46e-7)*T^2;

%Carriers v T
mu_n = (92*((T/300)^-.57))+(1268*(T/300)^-
2.33)/(1+(Nd/(1.3e17*(T/300)^2.4))^(.91*(T/300)^-.146)); %cm2 /(V*s)
% mu_n = mu_n*1.01;

mu_p = (54.3*((T/300)^-.57))+(406.9*(T/300)^-
2.23)/(1+(Na/(235e17*(T/300)^2.4))^(.88*(T/300)^-.146));
% mu_p = mu_p*1.01;

tau_n = 1e-7;
tau_p = 1e-7;

Area = cavity_length*cavity_width;
Dn = (k*T*mu_n/q);
Dp = (k*T*mu_p/q);
Ln = sqrt(Dn*tau_n);
Lp = sqrt(Dp*tau_p);
```

```
ni = A*((T/300)^(3/2))*((mnr*mpr)^(3/4))*exp(-(Eg-Eex)*q/(2*k*T));
% ni = ni*1.01;

Is_3O = Area*q*(((Dp/(Nd*Lp))+(Dn/(Na*Ln)))*(ni)^2);
% Is_3O = Is_3O*1.01;

VT = (Vt)*log(I./Is_3O+1)+I.*Rs;

end
```